

Tackling fluffy clouds: robust field boundary delineation across global agricultural landscapes with Sentinel-1 and Sentinel-2 Time Series

Foivos I. Diakogiannis^{a,1}, Zheng-Shu Zhou^a, Jeff Wang^a, Gonzalo Mata^b, Dave Henry^c, Roger Lawes^b, Amy Parker^d, Peter Caccetta^a, Rodrigo Ibata^e, Ondrej Hlinka^f, Jonathan Richetti^b, Kathryn Batchelor^b, Chris Herrmann^b, Andrew Toovey^b, John Taylor^g

^aData61, CSIRO, Kensington WA, Australia

^bA&F, CSIRO, Floreat WA, Australia

^cA&F, CSIRO, Melbourne, VIC 3030, Australia

^dCSIRO Space and Astronomy, Kensington WA, Australia

^eUniversity of Strasbourg, France

^fIM&T CSIRO, Australia

^gAustralian National University, School of Computing, ACT, Australia

Abstract

Accurate delineation of agricultural field boundaries is essential for effective crop monitoring and resource management. However, competing methodologies often face significant challenges, particularly in their reliance on extensive manual efforts for cloud-free data curation and limited adaptability to diverse global conditions. In this paper, we introduce PTAViT3D, a deep learning architecture specifically designed for processing three-dimensional time series of satellite imagery from either Sentinel-1 (S1) or Sentinel-2 (S2). Additionally, we present PTAViT3D-CA, an extension of the PTAViT3D model incorporating cross-attention mechanisms to fuse S1 and S2 datasets, enhancing robustness in cloud-contaminated scenarios. The proposed methods leverage spatio-temporal correlations through a memory-efficient 3D Vision Transformer architecture, facilitating accurate boundary delineation directly from raw, cloud-contaminated imagery. We comprehensively validate our models through extensive testing on various datasets, including Australia's ePaddocks™—CSIRO's national agricultural field boundary product—alongside public benchmarks Fields-of-the-World, PASTIS, and AI4SmallFarms. Our results consistently demonstrate state-of-the-art performance, highlighting excellent global transferability and robustness. Crucially, our approach significantly simplifies data preparation workflows by reliably processing cloud-affected imagery, thereby offering strong adaptability across diverse agricultural environments. Our code and models are publicly available at <https://github.com/feevos/tfcl>.

Keywords: convolutional neural network, semantic segmentation, Attention, vision transformer, change detection, time series, parcel boundaries, field boundaries

1. Introduction

The rise of digital agriculture has revolutionized how we monitor, manage, and optimize crop production. At the heart of this transformation lies the precise delineation of field boundaries, a critical component for maximizing efficiency in agricultural resource management. Accurate field boundary mapping significantly impacts applications such as crop yield estimation and food security assessments (de Wit and Clevers, 2004; Blaes et al., 2005; Matton et al., 2015). Historically, boundary mapping was a labor-intensive and error-prone process, leaving farmers and digital service providers grappling with inaccuracies. Today, however, frequent satellite observations from Sentinel-1 (S1) and Sentinel-2 (S2) provide opportunities to continuously refine these boundaries in sync with cropping cycles. This work harnesses these sensors to advance the frontiers of digital agriculture.

Traditional methods for extracting field boundaries, including edge-based, region-based, and hybrid techniques, have had varying degrees of success (Mueller et al., 2004; Turker and Kok, 2013; Yan and Roy, 2014; Graesser and Ramankutty, 2017). However, these approaches often falter in the face of noise, require extensive preprocessing, and struggle to adapt to diverse landscapes. The advent of deep learning presents a transformative solution, addressing these limitations by learning complex spatial and temporal features directly from satellite imagery.

Vision-based deep learning models offer robust and scalable boundary extraction, dynamically adapting to the evolving agricultural landscape (Persello et al., 2019; Waldner and Diakogiannis, 2020; Aung et al., 2020; Waldner et al., 2021; Wang et al., 2022; d'Andrimont et al., 2023; Tetteh et al., 2023). Despite these advancements, cloud cover remains a significant obstacle (Li et al., 2022), complicating boundary delineation from optical imagery. Conventional methods have relied on labor-intensive cloud removal or cloud-free composites, both costly and time-consuming. Moreover, approaches that depend on uncontaminated pixels are impeded by subjective cloud def-

¹foivos.diakogiannis@data61.csiro.au

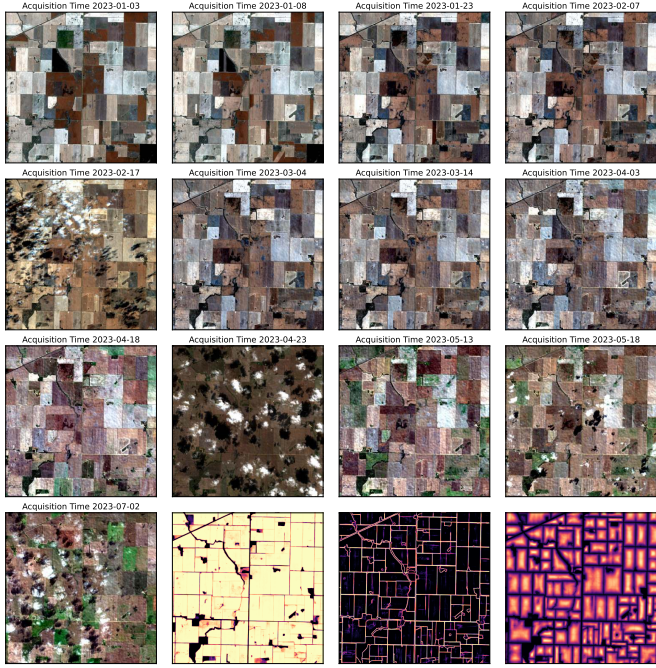


Figure 1: Our proposed algorithm can tackle inference on time series of input imagery, either pure S2 or combination of S2 and S1, and make predictions unaffected from sparse (S2) or dense (S1) cloud presence. This removes a significant barrier, which is the labor intensive process of acquiring cloud free imagery. This example showcases inference for the PTAiT3D model trained only on S2 over Australia.

initions and contamination thresholds, causing inconsistencies and errors. While the Sentinel-1 SAR sensor mitigates cloud interference, its spatial resolution has historically limited its effectiveness for precise boundary delineation.

Previous work addressed cloud contamination by selecting minimally clouded S2 imagery and employing consensus-based averaging techniques (Waldner and Diakogiannis, 2020; Waldner et al., 2021). This approach reduced cloud impacts but struggled under dense cloud conditions and failed to fully leverage temporal correlations, essential for accurate delineation.

Recent studies have exploited Satellite Image Time Series (SITS) to address some of these issues, yet they exhibit notable limitations:

- **Panoptic SITS models:** Garnot and Landrieu’s U-TAE family utilizes a Lightweight Temporal Attention Encoder (L-TAE) limited to the temporal axis, restricting its ability to fully capture spatio-temporal relationships (Sainte Fare Garnot and Landrieu, 2021a).
- **Large-scale rule-based pipelines:** Solano-Correa et al. (2022) proposed a country-scale mapping approach for Italy based on handcrafted features and morphological segmentation, lacking deep learning and manual cloud filtering, thus vulnerable under persistent cloud coverage.
- **Multimodal fusion networks:** Cai et al. (2023) introduced DSTFNet, combining very-high-resolution (VHR)

imagery and S2 time series through ConvLSTM and attention branches. Despite sharper delineation, the spatial and temporal modeling remains decoupled and dependent on VHR imagery not easily scalable.

- **Domain-adaptation frameworks:** FieldSeg-DA2.0 (Tian et al., 2024) merges Gaofen-2 (VHR) textures with S2 phenological information using adversarial domain adaptation, yet treats temporal dynamics separately.

These studies highlight two pervasive constraints: (i) a separable treatment of spatial and temporal dimensions, and (ii) dependence on either cloud-free inputs or external VHR imagery. In addition, there has been no explicit testing on cloud tolerance for field boundary delineation or land cover classification. To overcome these limitations, we propose a unified 3-D Vision Transformer architecture employing a novel 4D Patch Tanimoto Attention (PTA3D) mechanism that jointly encodes channel, spatial, and temporal dimensions in a single 4-D similarity map. This architecture inherently captures genuine spatio-temporal correspondences without cloud masking or reliance on auxiliary high-resolution data. Our approach processes raw S2 or S1 time series directly, optionally integrating both data streams through a cross-attention mechanism, enabling robust, cloud-tolerant delineation at continental scales.

With S2 time series, the model effectively addresses sparse cloud coverage by leveraging inherent spatio-temporal correlations. For S1 time series, unaffected by clouds, our model achieves spatial resolutions comparable to S2, producing precise and consistent boundary predictions. The ability to exploit embedded spatio-temporal relationships marks a significant leap forward in field boundary delineation accuracy and reliability.

This work introduces several key contributions:

1. A 3D Vision Transformer architecture specifically tailored to process SITS data, expanding upon our prior work in semantic segmentation (SSG2; Diakogiannis et al., 2024).
2. A memory-efficient and effective 3D vision attention mechanism designed explicitly for satellite image time series.
3. Two implementations: PTAiT3D for processing either S2 or S1 time series, and PTAiT3D-CA, integrating S2 and S1 data via cross-attention.
4. Demonstration of the model’s effectiveness when trained and tested on partially cloud-covered Sentinel-2 data (up to 40% cloud cover) and on Sentinel-1 data, which are immune to cloud coverage and provide comparable performance at the same spatial resolution (10m) as Sentinel-2-based approaches (Waldner et al., 2021), thus offering a robust alternative in densely clouded regions.
5. Demonstration of transferability across regions, by benchmarking against publicly available datasets: Fields of the World (FoTW; Kerner et al., 2024), the PASTIS dataset (Sainte Fare Garnot and Landrieu, 2021a), and the AI4SmallFarms

dataset (Persello et al., 2023), covering diverse agricultural landscapes and challenges.

6. A roadmap application for large-scale agricultural boundary delineation, with the application and validation of PTAViT3D across the Australian cropping regions, with the creation of the 2023 ePaddocks national product of Australia.

2. Methods

2.1. Data

Here we describe the datasets we used for evaluating our modeling approach. The first dataset is the ePaddocks dataset, provided by CSIRO, in 2021 version. In addition to that we also describe benchmark datasets that enables us to compare our algorithmic approach with baselines and state of the art in identical settings. We utilize the 2023 ePaddocks product as a benchmark against variable cloud conditions as well as, as a complete walk through / recipe for obtaining agricultural field boundaries at continental scale with detailed pipelines.

2.1.1. The ePaddocks field boundaries dataset of Australia

Sentinel 2: The development of our training dataset, based on Sentinel-2 imagery for field boundary detection, follows the methodology outlined in (Waldner et al., 2021). For completeness, we recap the process briefly. Training data were sourced from 2019 imagery, level L2A, and in particular bands blue (B2 490nm), green (B3 560nm), red (B4 665nm) and near-infrared (NIR 842nm). Additional imagery with 10% cloud tolerance was obtained for the same dates using the [Open Data Cube](#) (Accessed: 2023) Software. This new imagery was used after pre-training on the original data, serving as a fine-tuning procedure.

The creation of the annotated data was a model-assisted manual process. Initial field objects were derived through automated segmentation on six selected tiles (50JPL, 53HNC, 54HXE, 55HDA, 55HEE, 56JLQ) with clear-sky imagery. The output was refined by masking non-agricultural areas using CLUM (Catchment Scale Land Use of Australia; ABARES, 2016) and delineating fields via a meanshift algorithm (Michel et al., 2015). Parameter optimization was guided by Bayesian techniques (Snoek et al., 2012) against a sample of fields. This was the starting point for further manual edits and adjustments that ensured accuracy, significantly reducing the initial polygon count. This process yielded over 60,000 fields for training, validation, and testing.

To evaluate the performance of the 2023 ePaddocks product, we collected field boundaries across 67 test tiles, each approximately 1 km². These areas are a subset of the test set used in (Waldner et al., 2021) for the 2019 season. The 2023 annotation was conducted by our CSIRO team.

Sentinel 1 The Sentinel-1 mission, part of the European Copernicus Program, provides polar-orbiting, all-weather, day-and-night C-band radar imaging for land and ocean services. Sentinel-1A was launched on 3 April 2014, followed by Sentinel-1B on 25 April 2016. The default imaging mode, Interferometric Wide Swath (IW), captures imagery with a 250 km swath

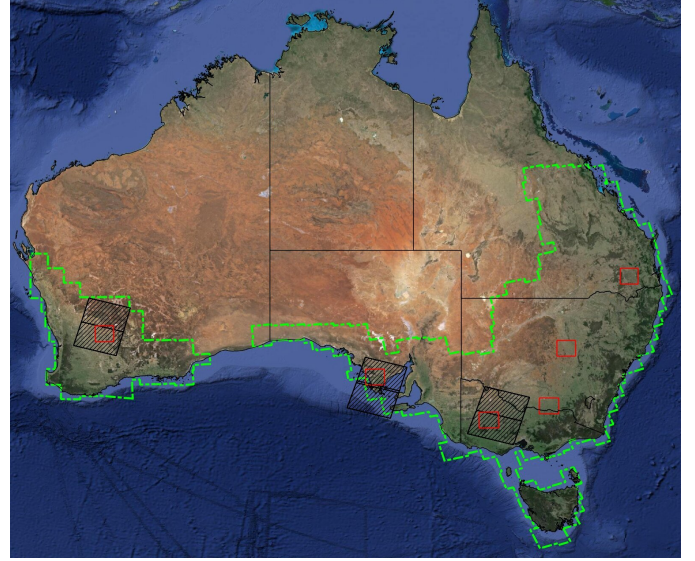


Figure 2: Inference and training area selection. Rectangles with red boundaries represent the training tiles (complete S2A scenes) where we have ground truth data. Footprints of Sentinel-1 scenes are represented with hashed black rectangles. Background imagery Map data ©2023 Google

at a spatial resolution of 5 m by 20 m. Equipped with dual polarization radars (VV+VH or HH+HV), Sentinel-1 delivers data that is essential for medium- to high-resolution applications, with routine coverage of Australia every 12 days since December 2016, enabling continental-scale land surface mapping and monitoring.

The availability of high-quality dual-pol Sentinel-1 IW data allows the use of dual-polarization Entropy/Alpha decomposition. These decomposition products provide more detailed information about scatterers compared to single-channel backscatter, improving the accuracy of landcover classification and segmentation (Cloude and Pottier, 1997; Zhou et al., 2017).

For this study, we selected Sentinel-1 dual-pol data in both SLC (Single Look Complex) and Ground Range Detected (GRD) formats, acquired over the testing sites between May and November 2019. Fig. 2 shows the footprints of Sentinel-1 scenes covering the three testing sites. The site in South Australia required one Sentinel-1 scene, while the others required two consecutive scenes to cover the areas of interest. Details of Sentinel-1 observations are provided in Table 1.

The Sentinel-1 SLC data were pre-processed using ESA’s Sentinel-1 Toolbox. The following steps were applied to each dual-pol VV+VH SLC product: applying the Precise Orbit File, removing thermal noise, radiometric calibration, S1 TOPS de-burst and merge, polarimetric speckle filtering, polarimetric decomposition, multi-looking, and terrain geometric correction (geocoding to a pixel spacing of 0.0002 degrees). After processing, adjacent scenes were mosaiced, and three dates were co-registered, resulting in a data stack ready for further analysis, including VV intensity, VH intensity, and three polarimetric decomposition parameters—alpha (α), anisotropy (A), and entropy (H)—using the Eigen-based dual-pol decomposi-

tion method (Cloude, 2007) (see Appendix A for details). Detailed processing steps are described in (Zhou et al., 2017; Mascolo et al., 2022; Zhou et al., 2023).

2.1.2. Benchmark datasets

To showcase transferability across regions, we compare our proposed methodology and benchmark it against established methods and datasets. We trained and evaluated models on the following datasets:

The **Fields of The World (FoTW)** dataset (Kerner et al., 2024) is a global-scale benchmark specifically designed for agricultural field boundary segmentation. It covers 24 countries across four continents, providing over 70,000 samples paired with semantic and instance segmentation masks aligned to multispectral Sentinel-2 imagery. Each FoTW sample includes two Sentinel-2 L2A cloud-filtered composites captured at contrasting dates within the same year, emphasizing the geographic and morphological diversity of fields, enabling robust cross-region assessments. We utilize FoTW solely for benchmarking purposes, evaluating our model on standardized test splits for selected countries without additional fine-tuning.

The **PASTIS** dataset (Sainte Fare Garnot and Landrieu, 2021a) was initially developed for panoptic segmentation tasks but also serves effectively for crop type semantic segmentation—a task closely related to field boundary delineation. The dataset provides rich Sentinel-2 time series data, ranging from 33 to 61 acquisitions, with partial cloud coverage. This makes PASTIS particularly suitable for evaluating our approach’s robustness to varying temporal dynamics and cloud conditions.

The **AI4SmallFarms** dataset (Persello et al., 2023) includes field outlines aligned to Sentinel-2 imagery for three distinct regions: Mekong Delta (Vietnam), Tonlé Sap (Cambodia), and West-Friesland (Netherlands). We specifically focus on the Vietnam and Cambodia subsets, as they present significant challenges due to their high cloud frequency—forcing reliance on sparse clear-sky observations—and highly fragmented landscapes with sub-hectare paddies separated by narrow earth dykes.

Since the AI4SmallFarms dataset is already included in FoTW using standard Sentinel-2 images at 10m resolution, we opted here to explore an alternative approach. Specifically, we assessed the algorithm’s performance on small farm fields using Sentinel-1 data combined with super-resolved Sentinel-2 imagery. The original S2 cloud-free composite provided by AI4SmallFarms was initially upsampled fourfold using the open-source Super Resolution Sentinel-2 (LDSR-S2) model (Donike et al., 2025). We recreated the ground truth for field extents, boundaries, and distance transforms (Diakogiannis et al., 2020; Waldner and Diakogiannis, 2020; Waldner et al., 2021) from the original reference polygons at this higher resolution. We emphasize that the super-resolution method applied is generative and may introduce minor inaccuracies specifically in the imagery rather than the ground truth.

Additionally, we enriched the dataset by complementing the Sentinel-2 imagery with Sentinel-1 time series, following procedures similar to those used for Australian tiles. Sentinel-1 IW images, in both GRD and SLC formats, acquired from 1 January to 28 February 2021 (descending orbit), consistent with

the original optical image acquisition period (Persello et al., 2023), were downloaded from the ASF data portal². Sentinel-1 data were processed into analysis-ready products using standard SNAP workflows on CSIRO’s HPC systems, resulting in a pixel spacing of 1e-4 degrees (EPSG 4326) and including normalized radar backscatter (Gamma0 VV and VH) and polarimetric decomposition parameters (alpha, Anisotropy, and Entropy), with radiometric terrain flattening and geometric terrain corrections applied using the 30m Copernicus global DEM.

2.2. Model architecture

This section describes the adaptation of the base model PTAViT developed for 2D inputs (Diakogiannis et al., 2024), for the case of time series of imagery. This can be a single type of input (S2 or S1) or a data fusion methodology (S1&S2) with cross (relative) attention. Both of these approaches share the same building block, the PTAViT3D Stage and utilize 3D hybrid convolutions.

2.2.1. Patch Tanimoto Attention 3D

Building upon our previously defined 2D attention method (Diakogiannis et al., 2024), we extend it here to handle the temporal dimension explicitly. Given that we have a limited number of time observations, we retain all individual time instances rather than grouping them into blocks. This allows a clear and detailed comparison at each individual time step. For completeness, we briefly discuss the time partitioning attention below, but readers interested in further details are encouraged to consult (Diakogiannis et al., 2024)³.

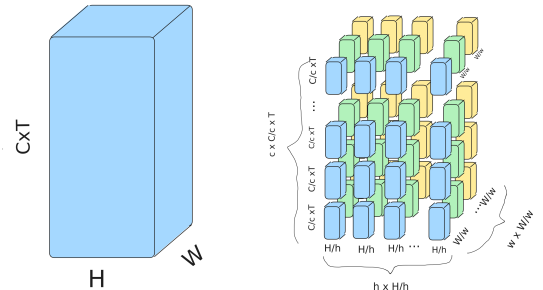


Figure 3: Schematic partitioning of a $C \times T \times H \times W$ tensor in $c \times t \times h \times w$ patches. Each patch has dimensions $(C/c) \times (T/t) \times (H/h) \times (W/w)$, where C are the channels of the original 3D tensor, T the time, H, W the height and width respectively. c, h, w are number of partitions in each dimension.

Figure 3 illustrates our method of partitioning a tensor with dimensions $C \times T \times H \times W$ (channels, time, height, width) into a set of $c \times t \times h \times w$ partitions. Each patch in this partition thus has dimensions $(C/c) \times (T/t) \times (H/h) \times (W/w)$, where c, T, h, w represent the number of partitions in each respective dimension, and $c \cdot T \cdot h \cdot w$ is their total number.

The Tanimoto similarity is defined as:

$$\mathcal{T}(\mathbf{q}, \mathbf{k}) = \begin{cases} \frac{\langle \mathbf{q} | \mathbf{k} \rangle}{\langle \mathbf{q} | \mathbf{q} \rangle + \langle \mathbf{k} | \mathbf{k} \rangle - \langle \mathbf{q} | \mathbf{k} \rangle} & \mathbf{q} \neq \mathbf{0} \text{ or } \mathbf{k} \neq \mathbf{0} \\ 0 & \mathbf{q} = \mathbf{k} = \mathbf{0} \end{cases} \quad (1)$$

²<https://search.asf.alaska.edu/>.

³<https://github.com/feevos/ssg2>.

Table 1: Acquisition dates and product numbers of Sentinel-1 observations for 3 sites

State	# Scenes	Acquisition Period (2019)	# Acquisition Dates	Sentinel-1 Products	
				GRD	SLC
WA (50JPL)	2	04/30-11/20	17	34	34
SA (53HNC)	1	05/09-11/29	18	18	18
VIC (54HXE)	2	05/01-11/21	18	36	36

Here, $\langle \mathbf{q} | \mathbf{k} \rangle$ denotes a form of inner product (tensor contraction) performed along selected dimensions of tensors \mathbf{q} and \mathbf{k} . Initially, both query (\mathbf{q}), key (\mathbf{k}), and value (\mathbf{v}) tensors have the shape $C \times T \times H \times W$. These are reshaped into smaller patches:

$$q_{C \times T \times H \times W} \rightarrow q_{c \times T \times h \times w \times (C/c) \times (H/h) \times (W/w)}$$

$$k_{C \times T \times H \times W} \rightarrow k_{c \times T \times h \times w \times (C/c) \times (H/h) \times (W/w)}$$

$$v_{C \times T \times H \times W} \rightarrow v_{c \times T \times h \times w \times (C/c) \times (H/h) \times (W/w)}$$

These smaller patches (see Fig. 3) serve as the building blocks for calculating Tanimoto similarity. Specifically, the similarity is calculated by contracting the tensor along the channel, height, and width dimensions (indices r, s, t) of these patches:

$$\langle \mathbf{q} | \mathbf{k} \rangle = \sum_{rst} q_{cFhw rst} k_{kTlm rst} \equiv \langle \mathbf{q} | \mathbf{k} \rangle_{cFhw kTlm} \quad (2)$$

$$\langle \mathbf{q} | \mathbf{q} \rangle = \sum_{rst} q_{cFhw rst} q_{cFhw rst} \equiv \langle \mathbf{q} | \mathbf{q} \rangle_{cFhw} \quad (3)$$

$$\langle \mathbf{k} | \mathbf{k} \rangle = \sum_{rst} k_{kTlm rst} k_{kTlm rst} \equiv \langle \mathbf{k} | \mathbf{k} \rangle_{kTlm} \quad (4)$$

The resulting Tanimoto similarity of q and k , has dimensions $\mathcal{T}(q, k)_{cFhw kTlm}$. Here $cFhw$ or $kTlm$ correspond to dimensions of channel partitions, time, height partitions and width partitions. The information of the 8-D coordinate similarity map, is contracted to 4D in two possible ways. We can either use a Linear matrix multiplication or, given that we want to increase the number of time observations during inference, to just use the mean value (reduces memory footprint) along the query dimensions:

$$\tilde{\mathcal{T}}(q, k)_{kTlm} = \sum_{cFhw} \mathcal{T}(q, k)_{cFhw kTlm} W_{cFhw} \quad (5)$$

$$\tilde{\mathcal{T}}(q, k)_{kTlm} = \frac{1}{N} \sum_{cFhw} \mathcal{T}(q, k)_{cFhw kTlm}, \quad (6)$$

where $N = \dim(cFhw)$ is the product of the first four dimensions of the query tensor, \mathbf{q} , and W_{cFhw} a weight matrix for the case of Linear matrix multiplication.

It should be noted that this similarity can be given causal structure, by multiplying element wise with a mask lower triangular matrix, m_{FT} along the time dimensions, i.e.

$$\mathcal{T}_{csl}(q, k)_{cFhw kTlm} = \mathcal{T}(q, k)_{cFhw kTlm} m_{FT} \quad (7)$$

where

$$m_{FT} = \begin{cases} 1, & \text{if } F \leq T \\ 0 & \end{cases} \quad (8)$$

and this is useful for forecasting applications of our methodology.

Finally, the attention layer is produced by element-wise multiplication of this similarity matrix, taking into account the time slot, with the values tensor, v , and re-arranging the patches to the original tensor shape, subject to the activation d2s:

$$\mathcal{A}(q, k, v)_{kTlmrst} = \text{d2s}(\tilde{\mathcal{T}}(q, k)_{kTlm} \odot v_{kTlmrst}) \quad (9)$$

The Attention map, $\mathcal{A}(q, k, v)$, upon reshaping, has dimensionality $C \times T \times H \times W$, and encapsulates all time, spatial and channel correlations that exist between query and key tensors to a patch resolution level of $c \times h \times w$, i.e. $\mathcal{A}(q, k, v) \in \mathbb{R}^{C \times T \times H \times W}$. Hereafter, we will refer to this attention map as Patch Tanimoto Attention 3D (PTA3D).

2.2.2. Limitations of separable channel-spatial-temporal similarity

In many Satellite Image Time-Series vision models the full 4-D similarity between query and key, $\mathbf{q}, \mathbf{k} \in \mathbb{R}^{C \times T \times H \times W}$, is approximated by three independent inner-products:

$$\langle \mathbf{q} | \mathbf{k} \rangle_{\text{channel}} = \sum_{j,k,t} q_{itjk} k_{itjk} \in \mathbb{R}^C, \quad (10)$$

$$\langle \mathbf{q} | \mathbf{k} \rangle_{\text{space}} = \sum_{i,t} q_{itjk} k_{itjk} \in \mathbb{R}^{H \times W}, \quad (11)$$

$$\langle \mathbf{q} | \mathbf{k} \rangle_{\text{time}} = \sum_{i,j,k} q_{itjk} k_{itjk} \in \mathbb{R}^T, \quad (12)$$

and then combined via broadcasting. However, as illustrated in Fig. 4, when two patterns occupy disjoint channels or time steps all of these separable terms vanish, even if a genuine spatiotemporal correspondence exists. In the example in Fig. 4 we plot two red (1, 0, 0) discs and two blue (0, 0, 1) discs that are spatio-temporally separated.

By contrast, our *Patch Tanimoto Attention 3D* (PTA3D) preserves cross-dimensional interactions. We first reshape the tensors (see also Fig. 3)

$$\mathbf{q} \in \mathbb{R}^{C \times T \times H \times W} \longrightarrow \mathbf{q} \in \mathbb{R}^{c \times T \times h \times w \times (C/c) \times (H/h) \times (W/w)},$$

(and similarly for \mathbf{k}, \mathbf{v}), so that each patch spans all four original axes. We then compute the Tanimoto similarity of each query-key patch pair via Eq. (1), yielding an 8-D tensor

$$\mathcal{T}(\mathbf{q}, \mathbf{k}) \in \mathbb{R}^{c \times T \times h \times w \times c \times T \times h \times w},$$

and finally contract the paired patch-coordinates (either by a small linear projection or by simple averaging). This retains true spatiotemporal matches without blowing up memory, as Fig. 5 shows. The result (Fig. 5) is a full $c \times T \times h \times w$ attention map that faithfully encodes all channel, spatial and temporal correlations at patch resolution, yet remains efficient on modern GPUs.

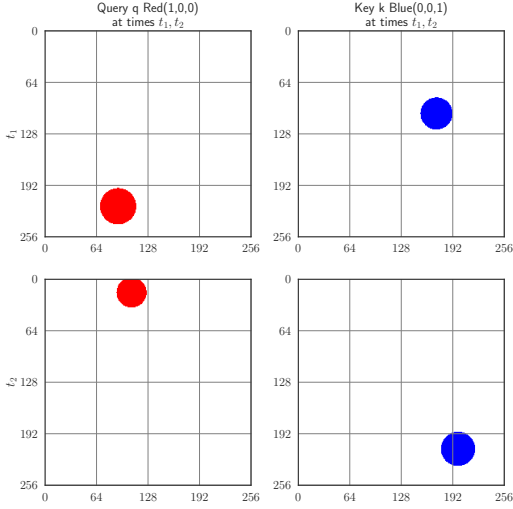


Figure 4: Query, q , and key, k , similarity between a red $(1, 0, 0)$ and a blue $(0, 0, 1)$ disjoint disks at different times t_1, t_2 . The element-wise multiplication that is used for time-channel-space separable attention results in 0 for all channels $(= (1 \cdot 0, 0 \cdot 0, 0 \cdot 1))$.

2.2.3. Feature extraction units

Following our previous work on the PTAViT architecture, we replace the 2D convolutions and patch Tanimoto Attention with their 3D equivalents presented here. These units build on MaXViT (Tu et al., 2022) by replacing the 2 blocks of attention with a single Attention block.

2.2.4. Single Input time series: UNet macro-topology

For modelling single input (S1 or S2) time series of observations, we adopt a PTAViT 2D model to account for 3D structure, by using the PTAViT3D Stages. Details for both the 3D Stage (Fig. 6(a)) and UNet macrotopology (Fig. 6(b)) of this implementation can be seen in Figure 6. We note that in this architecture, the encoder and decoder are symmetric, as this is depicted by the same number of stages used in the encoder and the decoder. Crucially, the Time dimension is kept along all of the blocks of the module, i.e. there is no pooling or dimensionality reduction along the time dimension. All exchange of information through various time snapshots is achieved with the 3D version of the attention, PTA3D. This is in contrast with the alteration of the spatial dimension that is gradually reduced in the encoder and increased again in the decoder.

At the end of the 3D features created, we attach another PTAViT3D stage before compacting the time dimension to create the final filtered multitasking segmentation predictions. The multitasking segmentation head is the standard we have used in our previous work developed in (Diakogiannis et al., 2020) and used in various semantic segmentation publications (Waldner and Diakogiannis, 2020; Diakogiannis et al., 2021; Waldner et al., 2021). This head predicts in a causal way the extent, boundaries and distance transform of each field (or class for the case of multiple classes segmentation).

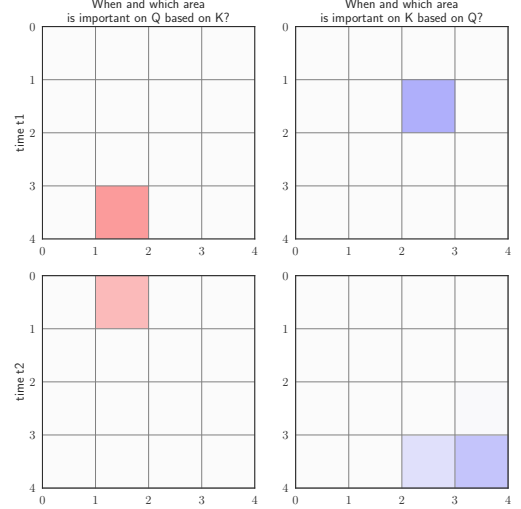


Figure 5: PTA3D emphasis maps for the example in Fig. 4, correctly identifying the matching patch across time space and channels.

2.2.5. S2&S1 feature fusion architecture

The fusion process is achieved with a dual encoder (without shared weights) single decoder architecture utilizing the 3D cross attention we present here. This is similar to the SSG2 base model architecture (Diakogiannis et al., 2024, see also Diakogiannis et al. 2021), however a crucial distinction is that now all time snapshots are compared with all other time instances. That is, the cross attention “sees” all relative time instances in order to assign emphasis (weighting) to a particular spatio-temporal location. This expands the scope of our previous work, that was developed for a set of observations where order along the sequence dimension was irrelevant. The creation of the segmentation masks from the extracted 3D features is similar to the UNet macrotopology as described above. Details can be seen in Fig 7. The hyper parameter configuration we follow is the same as in SSG2, 4 stages ([2,2,5,2]) for the encoder, and 3 for the decoder ([5,2,2]), starting from 96 initial features, which are doubled in every subsequent stage of the encoder architecture, and then halved for each subsequent stage of the decoder.

2.3. Loss function

For the loss function we use for all layers the multitasking approach we developed in (Diakogiannis et al., 2020), i.e. the Tanimoto with complement:

$$\mathcal{L}_{\mathcal{T}}(\mathbf{p}, \mathbf{l}) = 1 - \frac{1}{2} \left(\mathcal{T}(\mathbf{p}, \mathbf{l}) + \mathcal{T}(1 - \mathbf{p}, 1 - \mathbf{l}) \right) \quad (13)$$

where it is applied independently to the predictions of the extent, \mathbf{e} , boundaries, \mathbf{b} and distance transform, \mathbf{d} ground truth annotations:

$$\mathcal{L} = \frac{1}{3} \left(\mathcal{L}_{\mathcal{T}}(\hat{\mathbf{e}}, \mathbf{e}) + \mathcal{L}_{\mathcal{T}}(\hat{\mathbf{b}}, \mathbf{b}) + \mathcal{L}_{\mathcal{T}}(\hat{\mathbf{d}}, \mathbf{d}) \right) \quad (14)$$

2.4. Data pre-processing and Augmentation for Deep Learning pipeline

For the S1 data, the initial imperative step involves extracting areas corresponding to the S2 scenes and reprojecting them

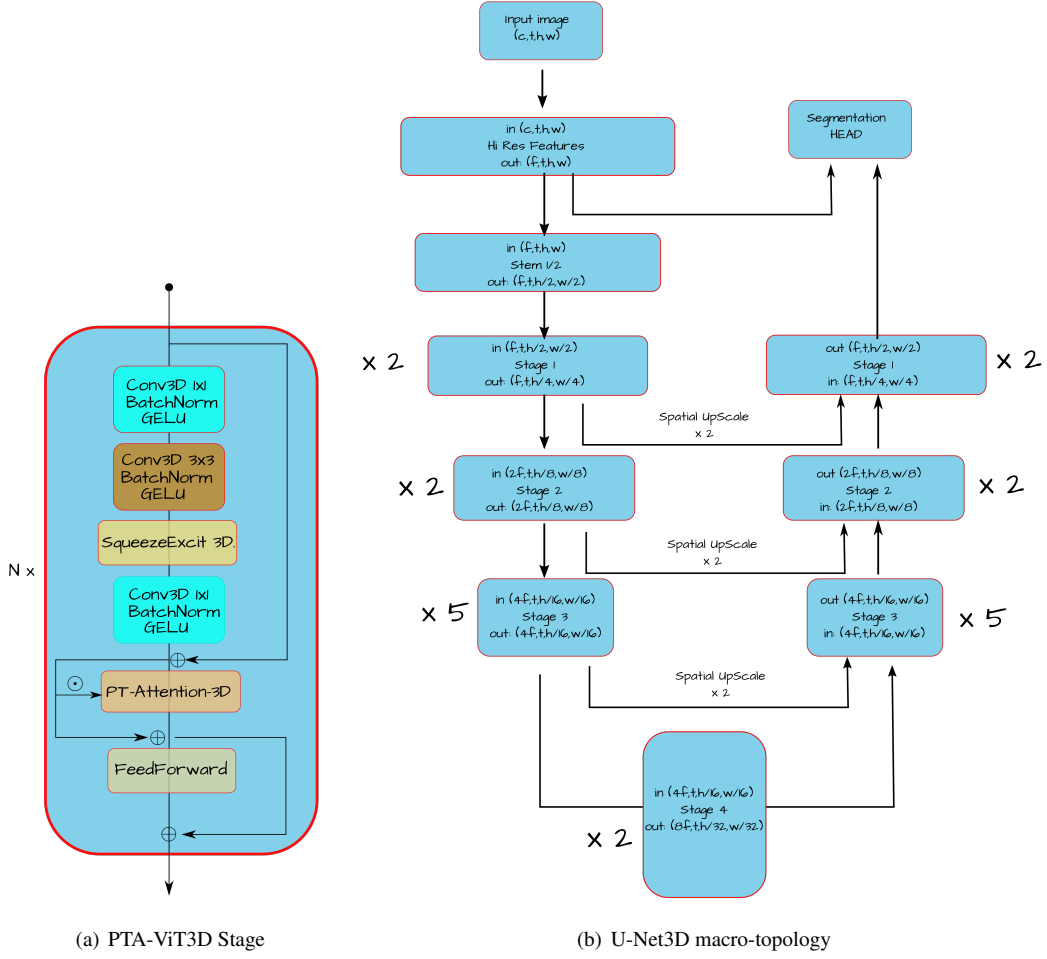


Figure 6: (a) Patch Tanimoto Attention ViT Stage. The Stage comprises a sequence of MBConv blocks, followed by Squeeze Excitation, Patch Tanimoto Attention and a FeedForward network. The architecture is defined by the number of these building blocks that are repeated. (b) The UNet3D macro-topology is symmetric in its encoder and decoder, which is reflected by the same number of stages used in the corresponding points of the Encoder and Decoder layers. In the Figure we show the Tiny configuration of [2,2,5,2,5,2,2] network.

to match the S2 pixel resolution. This alignment is essential because the Ground Truth labels are tailored to the spatial resolution of the S2 scenes.

The preprocessing of S1 data is conducted using the function `transform_s1` (Appendix B.1, Listing 1)). This function adjusts the first band, representing the incidence angle α , by converting its values from degrees to radians to standardize its range. Furthermore, it applies a symmetric logarithmic transformation to the VH and VV polarization bands, effectively expanding the dynamic range of these values, making them more suitable for neural network processing. This transformation is particularly beneficial for accommodating the stark contrasts between high magnitude values (VH and VV) and lower magnitude values (α , anisotropy, and entropy), thus enhancing stability during the learning phase. Subsequently, the data are standardized to achieve zero mean and unit variance.

The S2 dataset undergoes a similar standardization process to ensure zero mean and unit variance across all four bands. Given the constraints posed by GPU memory, training chips of size 128×128 pixels are extracted with a stride of 128 pixels.

This method ensures that the dimensions of the training chips remain compatible with the memory capacity of the GPUs utilized.

To further enhance the model’s generalization ability, a comprehensive suite of data augmentation techniques is employed. These techniques include equal probability selections from a set of geometric transformations. The array of transformations comprises horizontal and vertical flips, elastic transformations for perspective adjustments, grid distortions up to a limit of 0.4, and shift-scale-rotate operations with a shift limit of 0.25, a scale range from 0.75 to 1.25, and a full rotational freedom up to 180 degrees.

This augmentation strategy enriches the training dataset, thereby bolstering the robustness of the deep learning model. These transformations are implemented using the Albumentations library (Buslaev et al., 2020).

2.5. Evaluation Metrics

In order to quantify the performance of our algorithms, we evaluate metrics for the task of semantic segmentation, which

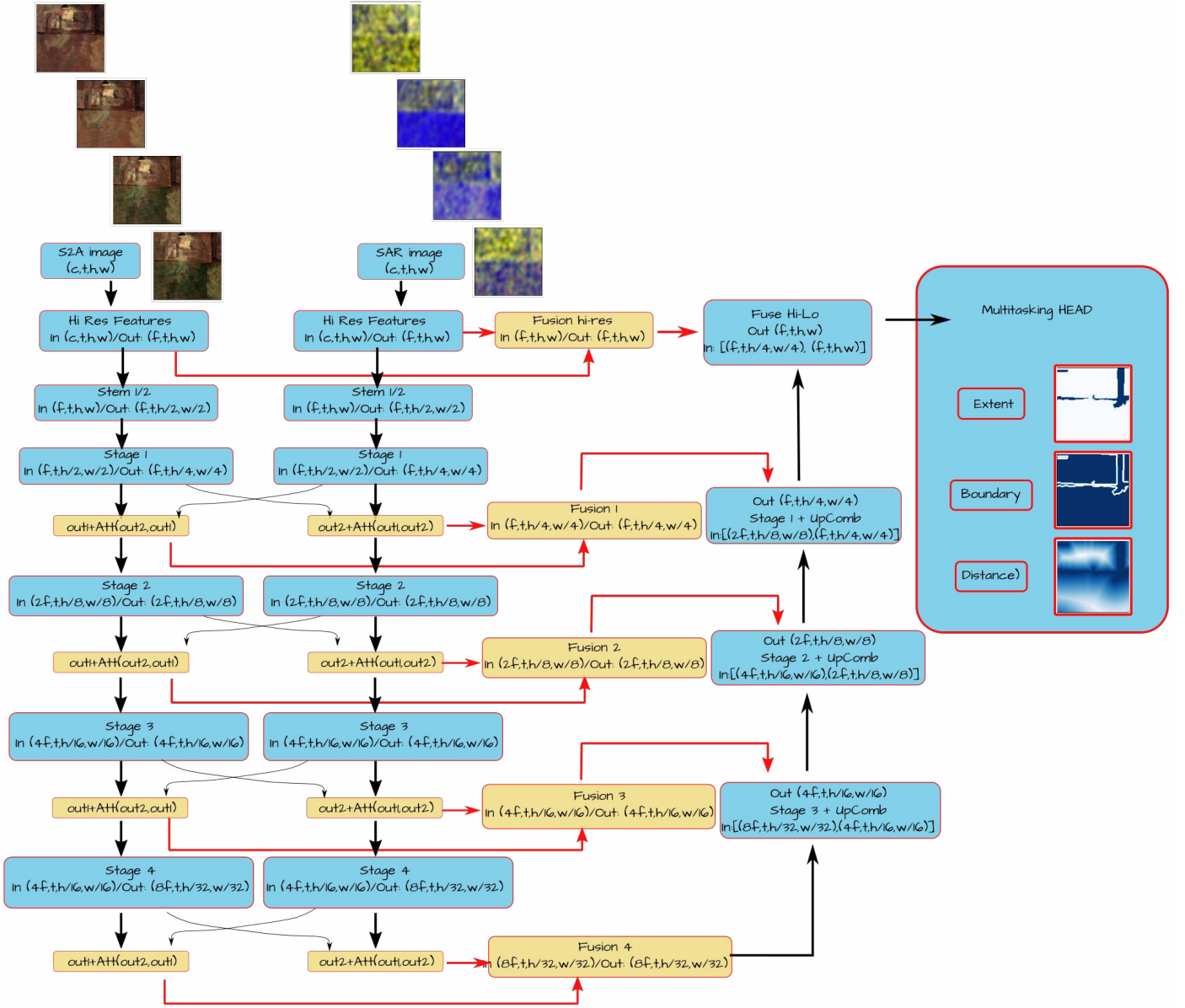


Figure 7: S2 (S2A) and S1 (SAR) Time Series Fusion architecture PTAViT3D-CA.

is the primary output of the PTAViT3D algorithm, as well as metrics that quantify the agreement between the boundaries (i.e. the polygon lines) that are created as a post processing step.

All of the evaluation metrics were based on calculation first of the confusion matrix with the use of the package PyCM (Haghighi et al., 2018). For the evaluation of the performance, we use the metrics described in Sections 2.5.1, 2.5.2 and 2.5.3.

2.5.1. Segmentation Evaluation Metrics

The metrics used for the quantification of semantic segmentation are the Matthews Correlation Coefficient (MCC), Intersection over Union, and Oversegmentation (FOR) and Under-segmentation (FDR) rates.

Matthews Correlation Coefficient. The Matthews Correlation Coefficient (Matthews, 1975) in its multiclass version (Gorodkin, 2004), defined by a $K \times K$ confusion matrix, C_{ij} , where K is the number of classes, is given by:

$$MCC = \frac{cs - \sum_{i=1}^K p_i t_i}{\sqrt{(s^2 - \sum_{i=1}^K p_i^2)(s^2 - \sum_{i=1}^K t_i^2)}} \quad (15)$$

where

$$\begin{aligned}
t_i &= \sum_{j=1}^K C_{ji} \quad \text{represents the actual occurrence count of class } k, \\
p_i &= \sum_{j=1}^K C_{ij} \quad \text{indicates how many times class } k \text{ was predicted,} \\
c &= \sum_{i=1}^K C_{ii} \quad \text{is the total number of correct predictions,} \\
s &= \sum_{i=1}^K \sum_{j=1}^K C_{ij} \quad \text{is the overall sample count.}
\end{aligned}$$

MCC ranges from $[-1,1]$ in the binary case, where a value of 1 suggests maximum performance. For the multiclass case the lower value $\in [-1,0]$.

Intersection over Union. For two one-hot encoded binary predictions P and L of shape $N \times H \times W$, where N is the number of classes, H and W the height and width respectively, we define the mean Intersection over Union, via the (fuzzy) set operations of intersection and union as:

$$\text{mIoU} = \frac{1}{N} \sum_{i=1}^N \frac{\sum_{j,k} \min(P_{ijk}, L_{ijk})}{\sum_{j,k} \max(P_{ijk}, L_{ijk})} \quad (16)$$

For binary one dimensional masks, we use the following definition:

$$\text{IoU} = \frac{TP}{TP + FP + FN} \quad (17)$$

2.5.2. Oversegmentation and Undersegmentation Rates

In the evaluation of segmentation algorithms, it is crucial to quantify the extent to which the predicted segments either overestimate or underestimate the actual segments. Two metrics commonly used for this purpose are the False Discovery Rate (FDR) (Benjamini and Hochberg, 2018) and the False Omission Rate (FOR, Powers, 2011).

False Discovery Rate (FDR). The False Discovery Rate (FDR) measures the proportion of false positives among the predicted positives. In the context of segmentation, it quantifies the extent of oversegmentation, i.e., the degree to which the predicted segmentation includes areas outside the ground truth segmentation. Mathematically, it is defined as:

$$\text{FDR} = \frac{|A \cap \bar{B}|}{|A|} \quad (18)$$

where A is the set of predicted positive pixels, \bar{B} is the complement of the ground truth positive pixels, and $|\cdot|$ denotes the cardinality (area) of a set.

False Omission Rate (FOR). The False Omission Rate (FOR) (Powers, 2011) measures the proportion of false negatives among the predicted negatives. In the context of segmentation, it quantifies the extent of undersegmentation, i.e., the degree to which

the predicted segmentation misses areas within the ground truth segmentation. Mathematically, it is defined as:

$$\text{FOR} = \frac{|\bar{A} \cap B|}{|\bar{A}|} \quad (19)$$

where \bar{A} is the complement of the set of predicted positive pixels, B is the set of ground truth positive pixels, and $|\cdot|$ denotes the cardinality (area) of a set.

These metrics provide a detailed understanding of the segmentation performance by separately evaluating the extent of oversegmentation and undersegmentation, thereby offering more granular insights compared to traditional metrics like Intersection over Union (IoU).

2.5.3. Boundary Evaluation Metrics

For the evaluation of polygon agreement, we use the Mean Surface Distance, the Hausdorff Distance, and, for the case of the AI4SmallFarms dataset, the PoLiS distance.

Mean Surface Distance (MSD). The Mean Surface Distance (MSD) is a metric used to evaluate the average distance between the surfaces of two geometries. In the context of polygon boundaries, MSD provides a measure of how closely two boundaries align with each other by averaging the minimum distances between the vertices of one polygon to the vertices of the other polygon. This metric is particularly useful for comparing the overall proximity of two shapes without being overly sensitive to outlier distances.

Let $X = \{x_1, x_2, \dots, x_{N_x}\}$ and $Y = \{y_1, y_2, \dots, y_{N_y}\}$ be the sets of vertices of two polygons. The pairwise distance matrix D between these vertices is computed using the Euclidean distance:

$$D_{ij} = \|x_i - y_j\|_2 \quad \text{for } i = 1, 2, \dots, N_x \quad \text{and } j = 1, 2, \dots, N_y$$

The MSD is then calculated as the average of the mean of the minimum distances from each vertex in X to the vertices in Y , and the mean of the minimum distances from each vertex in Y to the vertices in X :

$$\text{MSD}(X, Y) = \frac{1}{2} \left(\frac{1}{N_x} \sum_{i=1}^{N_x} \min_j D_{ij} + \frac{1}{N_y} \sum_{j=1}^{N_y} \min_i D_{ij} \right)$$

Hausdorff Distance. The Hausdorff Distance is a metric that measures the greatest distance from a point in one set to the closest point in another set. It provides a measure of the discrepancy between two sets of points and is particularly sensitive to outliers. For two polygon boundaries X and Y , the Hausdorff Distance d_H is defined as:

$$d_H(X, Y) = \max \left\{ \sup_{x \in X} \inf_{y \in Y} \|x - y\|_2, \sup_{y \in Y} \inf_{x \in X} \|y - x\|_2 \right\}$$

where sup and inf denote the supremum and infimum, respectively. In practical terms, the Hausdorff Distance is computed as the maximum of the directed Hausdorff distances from X to

Y and from Y to X . The directed Hausdorff distance d_H^d from X to Y is given by:

$$d_H^d(X, Y) = \max_{x \in X} \min_{y \in Y} \|x - y\|_2$$

Thus, the Hausdorff Distance is calculated as:

$$d_H(X, Y) = \max \{d_H^d(X, Y), d_H^d(Y, X)\}$$

Both the MSD and Hausdorff Distance provide valuable insights into the similarity and alignment of polygon boundaries, with the MSD offering an average-based measure and the Hausdorff Distance highlighting the most significant deviations.

Polygon Line-to-Segment distance (PoLiS). The *PoLiS* metric (Avbelj et al., 2015) evaluates the similarity of two closed polygon boundaries by averaging *vertex-to-edge* distances, instead of the usual *vertex-to-vertex* formulation. For each vertex of one polygon the shortest orthogonal distance to the *edges* (line segments) of the opposite polygon is measured, making *PoLiS* robust to different vertex samplings of the same curve and resilient to small topological artefacts such as self-intersections or micro-slivers.

Let $P = \{p_1, \dots, p_{N_P}\}$ and $Q = \{q_1, \dots, q_{N_Q}\}$ denote the ordered vertex sets of two polygons, and let ∂Q be the piecewise linear boundary of Q (i.e. its set of edges). The *directed* *PoLiS* from P to Q is the mean vertex-to-edge distance

$$d_{\text{PoLiS}}(P \rightarrow Q) = \frac{1}{N_P} \sum_{i=1}^{N_P} \text{dist}(p_i, \partial Q),$$

$$\text{dist}(p_i, \partial Q) = \min_{e \in \partial Q} \text{dist}(p_i, e),$$

where $\text{dist}(p_i, e)$ is the Euclidean distance from vertex p_i to edge e . The *symmetric* *PoLiS* used in this work is the average of the two directed values,

$$\text{PoLiS}(P, Q) = \frac{1}{2} (d_{\text{PoLiS}}(P \rightarrow Q) + d_{\text{PoLiS}}(Q \rightarrow P)).$$

Because every vertex contributes equally and deviations are measured relative to the exact opposite boundary, *PoLiS* strikes a useful balance: it is less sensitive to single outliers than the Hausdorff distance, yet more discerning than purely vertex-based averages such as the MSD when one polygon is over- or under-sampled. In this work we use *PoLiS* in the object level evaluation of the AI4SmallFarms benchmark, to compare with provided baselines by Persello et al. (2023).

Polygon Matching Algorithm. For the case of the AI4SmallFarms and ePaddocks datasets, we adopted a unified polygon matching algorithm to ensure consistency in boundary evaluation metrics. The predicted extent masks were initially vectorized and topologically repaired. Each valid geometry was then matched to a single ground-truth polygon (the reference polygon with the highest Intersection over Union (IoU)), provided the IoU exceeded a threshold of 10^{-3} . This one-to-one assignment ensures every boundary metric evaluation refers to genuine true-positive polygon pairs, preventing double-counting.

Table 2: Experiment matrix (✓ = dataset used, ✗ = not used).

Task	ePaddocks	FoTW	PASTIS	AI4SmallFarms
Sparse clouds	✓	✗	✗	✗
S2 vs. S1	✓	✗	✗	✗
S2&S1 fusion	✓	✗	✗	✓
3-D vs. 2-D	✓	✗	✗	✗
Transferability	✗	✓	✓	✓
Continental Product	✓	✗	✗	✗

For each matched polygon pair, relevant boundary evaluation metrics were computed. Specifically, we calculated the symmetric Polygon Line-to-Segment (*PoLiS*) distance by averaging the vertex-to-edge distances in both directions for the AI4SmallFarms dataset, precisely following the definition by (Avbelj et al., 2015), so we can compare our results with the (Persello et al., 2023) baselines. For the ePaddocks dataset, we employed the Hausdorff Distance and Mean Surface Distance (MSD), which measure the greatest boundary discrepancies and average boundary deviations, respectively. Polygons unmatched in this process (false positives or omissions) were accounted for within the pixel-level confusion matrix but excluded from boundary-specific metrics. This procedure ensures comparability across datasets irrespective of raster boundary thickness or spatial resolution.

2.6. Experimental Design

In this study, we aim to address four key research questions to comprehensively evaluate the performance, robustness, and applicability of our methodology:

1. *Cloud contamination effects.* We first assess how cloud cover impacts the algorithmic performance, focusing on two distinct scenarios: (i) sparse cloud cover conditions with Sentinel-2 (S2) Satellite Image Time Series (SITS), detailed in Section 3.1.1, and (ii) dense cloud coverage scenarios where spatial resolution from Sentinel-1 (S1) time series predictions is critical, as discussed in Section 3.1.2. Both analyses leverage the ePaddocks dataset.

2. *Sensor modality comparison.* We then compare different sensor modalities and modeling approaches. Specifically, we evaluate:

- Sentinel-2 SITS against Sentinel-1 SITS, using the ePaddocks dataset (Section 3.2.1), and
- 3D versus 2D versions of our model, along with the joint modeling of Sentinel-2 and Sentinel-1 SITS. These evaluations are conducted using both the ePaddocks and AI4SmallFarms datasets (Section 3.2.2).

3. *Generalization and benchmarking.* To assess the generalizability of our modeling approach, we conduct experiments across multiple geographic regions and benchmark against established baseline methods. Our evaluations use three publicly available benchmark datasets: (i) Fields of the World (FoTW)

(Kerner et al., 2024), (ii) Pastis (Sainte Fare Garnot and Landrieu, 2021a), and (iii) AI4SmallFarms (Persello et al., 2023). This comparative analysis, detailed in Sections 3.3.1, 3.3.2, and 3.3.3, allows direct assessment of our PTAViT3D model against existing methodologies under matched conditions.

4. Continental-scale application. Finally, we showcase the practical application and scalability of the PTAViT3D model at a continental scale. Specifically, we apply our model across Australia for the creation of the ePaddocks 2023 national product (Section 3.4). This section highlights detailed product validation and important algorithmic considerations necessary for operational use.

Table 2 summarizes the datasets employed in each experimental scenario. Due to computational constraints, experiments with the ePaddocks dataset for validation purposes utilized only two Sentinel scenes each for training and validation. The final test results and visualizations are derived from independent scenes outside the training and validation sets. For comprehensive national-scale results, the full ePaddocks product employed training on six Sentinel-2 tiles.

Given that ePaddocks is not publicly available, we validated our methodology against an established baseline by retraining the FracTAL ResNet proposed by Diakogiannis et al. (2021). This baseline has previously been successfully applied to field boundaries (Waldner et al., 2021) and validated independently across multiple datasets (Wang et al., 2022; Tetteh et al., 2023).

3. Results

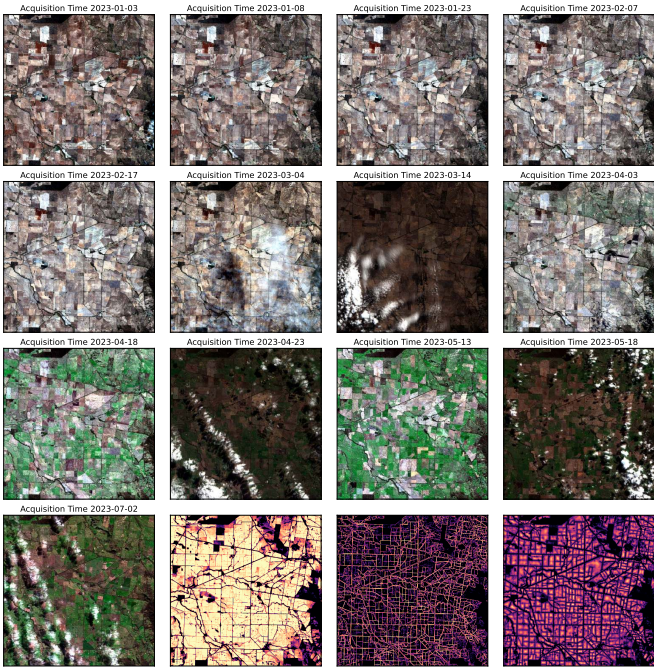


Figure 8: Example of inference on partially clouded imagery (selection of S2A imagery with cloud tolerance $\leq 10\%$), natural color, ePaddocks dataset.

3.1. Tackling sparse clouds

In this section we are trying to address the question qualitatively using sourced imagery over Australia. Given that the way we source data through the Open Data Cube (ODC) API we can only select a cloud percentage, that relates to the whole scene coverage and not individual pixels, as well as the fact that deep learning models see a wide field of view (not just pixels) to make a decision, it is very hard to quantify precisely contaminated pixels in the field of view. Our best hope is to show examples where the requested input imagery (for the case of optical data) was selected with a cloud coverage tolerance. We note that different cloud cover tolerances give in general different number of time series of observations. This affects the overall performance, as the general rule is that the more time observations we use the better the performance (Diakogiannis et al., 2024). In our approach, we request through the ODC API up to a maximum number of S2 tiles, within a given cloud tolerance, and we keep the ones that have the least cloud contamination and nodata ratio greater than 70%. The key idea in going around the problem of sparse cloud coverage is that clouds move, and within an extended time series, all ground surface regions will be revealed irrespective of partial occlusion due to cloud contamination in individual time instances.

3.1.1. S2 Solution

Here, we show two qualitative examples of inference, on a time series of 13 S2A tiles. These were sourced by requesting cloud coverage tolerance up to 10% for the whole scene. In figures Fig. 1 and Fig. 8 we show inference on a zoomed in area that has partially clouded images. By visual inspection of the predictions in these two cases, we see that there is no visible effect of the partially clouded areas on the predictions masks. We note that this is in stark contrast with the work of (Aung et al., 2020) where the Authors there used also time series of input images into their spatio-temporal modeling: they report performance degradation in areas obscured by cloud. This can potentially be attributed in their treatment of time series of S2 images as well as the small number of time instances (they used three instances). In their work they consume time series via concatenation of the input images along the channel dimension, i.e. there is no explicit 3D structure into the deep learning modeling approach.

In comparison with our previous work (Waldner and Diakogiannis, 2020; Waldner et al., 2021), where we were aggregating (averaging) predictions across various dates to achieve consensus, the proposed work here, removes significant overhead and compute, by avoiding sourcing, storing and averaging the predicted results. It also performs better (Fig. 13, Table 4, comparison with the FracTAL baseline Waldner et al. 2021, see also Tetteh et al. 2023) due to utilizing the correlation between various time instances of the same areas something that is not possible at the consensus level which is a post processing step.

How much cloud is too much cloud? To address this question, we sourced imagery for the test set of 67 tiles across the cropping area in Australia, using the OpenDataCube (ODC) API at varying levels of cloud coverage tolerance. The API allows specifying cloud coverage within intervals, so we selected

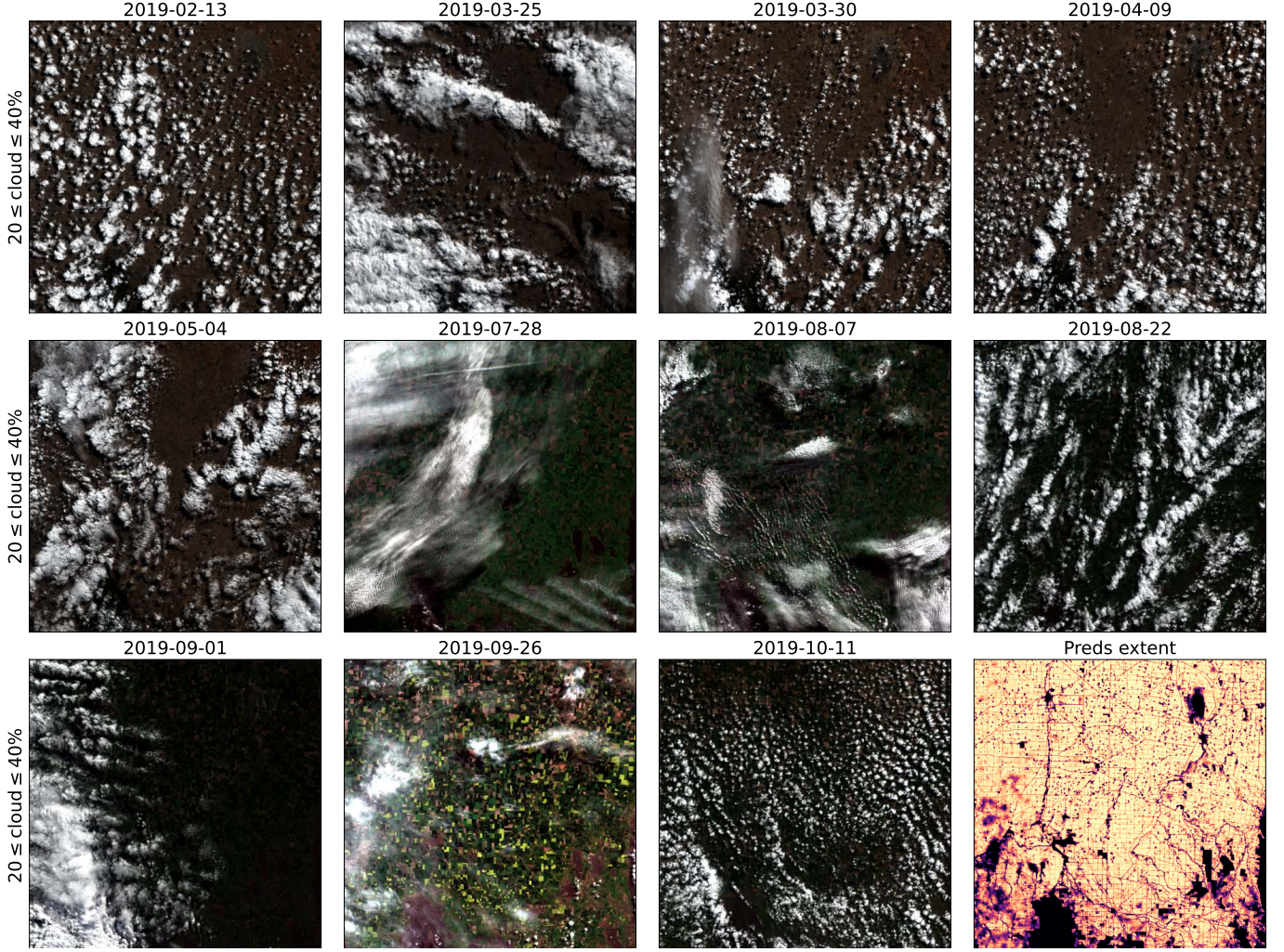


Figure 9: Example of sourced imagery with up to 20% to 40% cloud tolerance. We also visualize the extent predictions, ePaddocks dataset.

$[0, 20]\%$, $[0, 50]\%$, and $[20, 50]\%$. We also set upper bounds on the number of time instances used, at 16 and 32.

Table 3 shows the numerical performance in terms of IoU on the raster predictions. We observe a degradation in IoU performance between the $[0, 20]\%$ and $[20, 50]\%$ cloud coverage intervals when the maximum number of time instances is limited to 16, with IoU dropping from $\sim 0.8 \pm 0.2$ to $\sim 0.6 \pm 0.3$. This pattern is consistent whether the maximum number of time instances is 16 or 32. However, when the lower cloud coverage is fixed at 0, the performance between the $[0, 20]\%$ and $[0, 50]\%$ intervals remains nearly identical (within error bars).

To fully appreciate the effectiveness of our algorithm’s cloud tolerance, we also visualize sourced imagery from S2 tile 54HXX within the $[20, 40]\%$ (Fig 9) interval, alongside the corresponding predictions (Fig 10). As seen, there is some degradation when input imagery is restricted to 20-40% cloud coverage, but the results remain practically useful.

Cloud Coverage (%)	max Time Instances	$\langle \text{IoU} \rangle$
$[0, 20]$	16	0.79 ± 0.21
$[0, 50]$	32	0.77 ± 0.22
$[20, 50]$	16	0.5818 ± 0.3005
$[20, 50]$	32	0.5824 ± 0.2999

Table 3: Segmentation IoU values for different cloud coverage tolerance intervals.

3.1.2. S1 Solution

Here we again utilize the ePaddocks dataset. In areas that are mostly covered with clouds and it is not realistic to anticipate partial cloud cover, our S1 proposed algorithmic pipeline offers competitive results and a viable solution. Indeed our new model, PTAViT3D that consumes S1 time series performs on par with the baseline 2D FracTAL algorithm (Table 4) that was trained on higher spatial resolution of optical S2 imagery. In Figure 11 we visualize inference examples for the Algorithm PTAViT3D trained on time series of S1 images (16 time instances). From left to right we visualize the corresponding S2

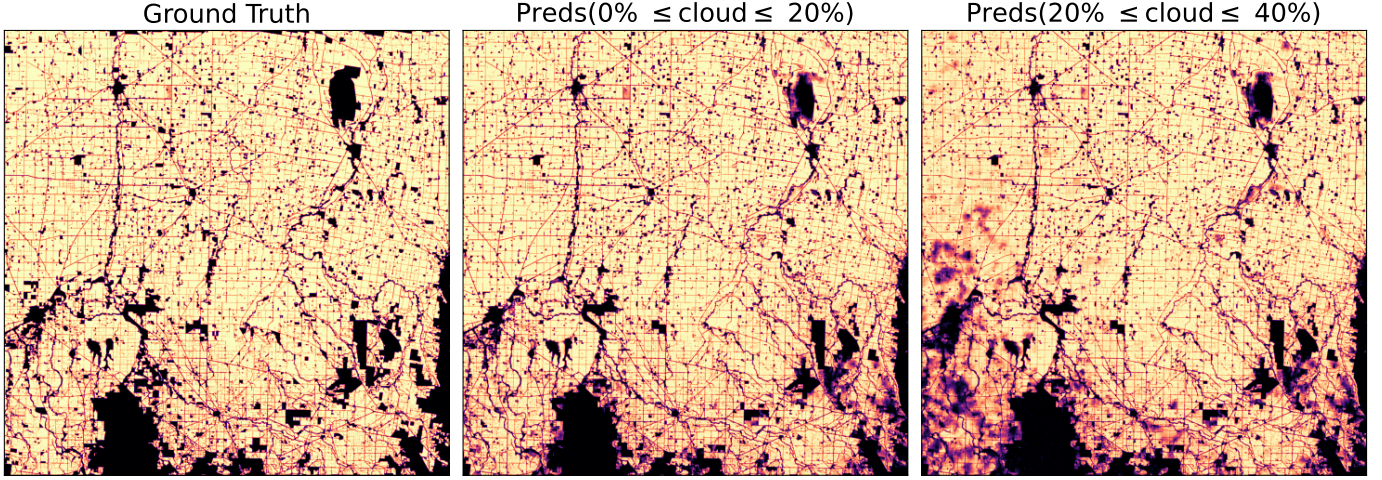


Figure 10: Comparison of inference for sourced time series of S2 at varying levels of cloud tolerance.

scene, the S1 scene (bands VH , VV , anisotropy A , average across all times), the extent density prediction, e , the bounds density prediction, b , the Distance transform, d , as well as the agreement with the Ground Truth fields.

It can be seen (Figures 11, 15) that the quality of the predictions is of high standard following closely the algorithmic results of the algorithm trained on the higher spatial resolution S2 data. In Figure 11 we visualize the agreement between the predicted field boundaries and the ground truth.

One very interesting result is that the spatial resolution of the predicted labels, is not close to the static single date input imagery as can be seen in Figure 15. That is, the algorithm, through the inclusion of additional time information, learns to effectively upscale the predicted labels to the level of the ground truth pixel resolution. In Figure 15 we show the performance on the scale of a single chip, of shape 128×128 . In the top row, from left to right we provide the corresponding S2 imagery (that is not seen from the PTAiT3D S1 algorithm), the average across all times S1 (bands VH , VV and A), the predicted extent and boundary layers as well as the Ground Truth (that corresponds to the S2 image resolution). In the next 2 rows we visualize all possible combinations of triplets for the 5 S1 bands, for the last date. It can be seen that the detail level of the ground truth masks cannot be deduced from a single image, nor the time averaged signal.

We also note that the visualization quality of the S1 predictions can be improved significantly by utilizing more data. The visualizations shown here were created by training on only two scenes, and testing on a separate test tile.

3.2. Sensor Modality analysis

How does model performance is affected with different kind of inputs. Here we analyse S2 vs S1 inputs performance, 3D vs 2D vs joint S2&S1 training.

3.2.1. S2 vs S1 inputs for field delineation

We compare the performance between S2 and S1 models using the ePaddocks dataset. In Fig. 12 we plot validation metrics for both 3D and 2D models trained on only S2 imagery (top panel) as well as on only S1 imagery (bottom panel). For the S2 imagery the 3D model consumes 4 cropping season time observations, while the S1 model consumes 16 time instances within the same time span. In both 2D and 3D cases the Sentinel 2 inputs provide a stronger signal for field boundary extraction. It is to be anticipated that due to the higher resolution S2 would perform better, however the increased time resolution of S1 could provide a counter balance in performance as we know that performance increases with the number of time steps (Diakogiannis et al., 2024). Despite the lower score, the 3D S1 model achieves excellent performance to be useful as a tool in areas where there is dense throughout the year cloud coverage, but it lags behind the S2 observations. We note that the performance of the PTAiT3D model with S1 inputs is on par with the FracTAL ResNet baseline (Table 4) which is trained on 2D cloud free S2 images.

3.2.2. 3D vs 2D vs Joint S1&S2

For the case of the ePaddocks dataset, in Fig. 13 we provide evolution plots on the validation split of the dataset for 3D models (top panel) as well as 2D models (bottom panel). The S2 and S2&S1 3D models are evaluated with 4 time inputs, while the S1 3D model with 16 time inputs. As expected, the time series (3D) models outperform their 2D counterparts in all cases. The evolution of the model S2S1 3D can be seen in the same Figure.

We observe that the model that consumes both S2 and S1 features converges faster to optimality, however after approximately 200 epochs the two models become similar in performance, showing that the 3D model trained on S2 only is a practical cost effective alternative to the S2& S1. The choice be-

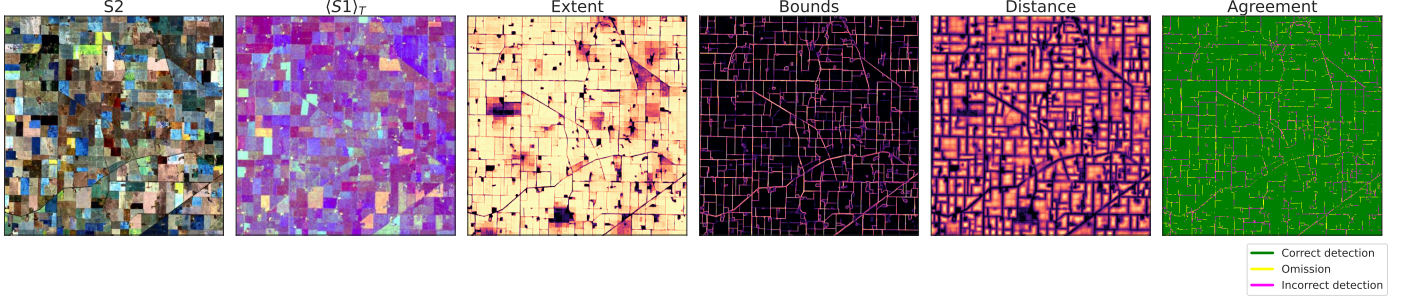


Figure 11: Example inference results from the PTAViT3D model using Sentinel-1 (S1) time series as input (16 temporal instances). The figure illustrates model outputs for extent, bounds, and distance layers. The final panel (“Agreement”) explicitly compares the inferred field boundaries against the Ground Truth, highlighting areas of correct detection, omissions, and incorrect detections.

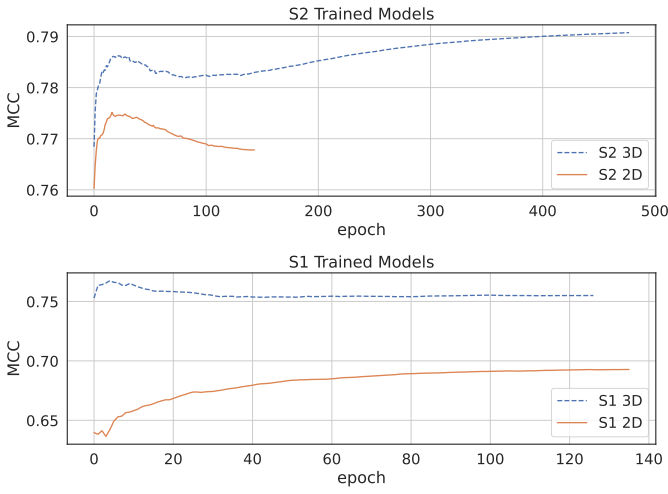


Figure 12: Validation MCC evolution. The 3D models are evaluated with 4 time inputs. The focus is comparing S2 and S1 quality as discriminative features.

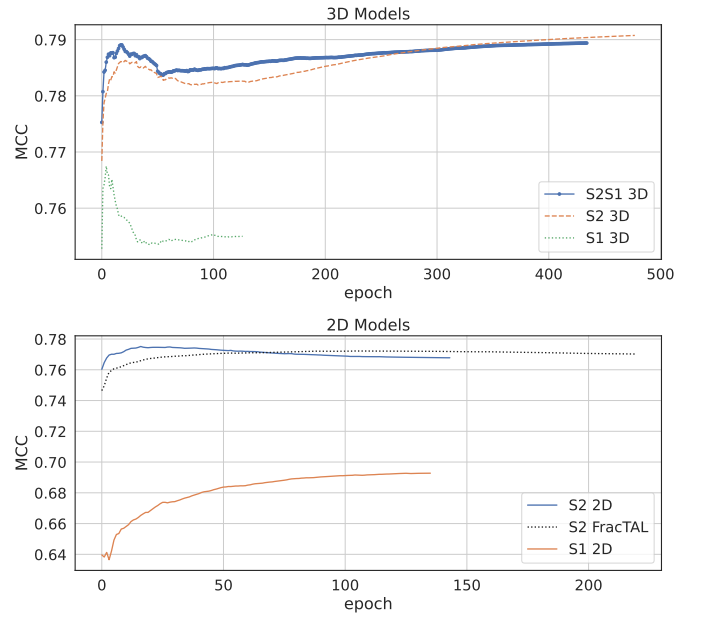


Figure 13: As in Fig 12 with focus on comparing 3D architectures with 2D ones.

tween the two boils down to the percentage of cloud coverage as well as computational resources available, given the S2& S1 converges faster to higher performance.

Finally in Table 4 we present the numerical values from all the models, where it can be seen that the ranking is $S2\&S1\ 3D \geq S2\ 3D \geq S2\ 2D \geq S1\ 3D \approx \text{FracTAL}\ S2 \geq S1\ 2D$. This ranking is to be expected, as: a) The S1 has lower spatial resolution than S2, and b) the combination of features from both sensors improves discrimination of the field boundaries.

Model	NTimes	Epoch	MCC	Precision	Recall	F1	IoU
S2S1 3D	4	434	0.79	0.89	0.91	0.89	0.81
S2 3D	4	477	0.79	0.88	0.92	0.89	0.81
S1 3D	16	4	0.77	0.84	0.95	0.88	0.79
S2 2D	1	16	0.78	0.84	0.95	0.88	0.79
S1 2D	1	104	0.69	0.82	0.88	0.84	0.73
FracTAL S2	1	108	0.77	0.84	0.95	0.88	0.79

Table 4: Evaluation Metrics for different models (i.e. different sensor modalities) on the ePaddocks validation set (Australia). The best numerical values are designated with **bold** font.

For the case of the AI4SmallFarms dataset, that consumes

a single S2-SR input image and a time series of S1 models, the situation of performance is different, indicating that the S1 time series can add significant value to the modeling. Fig. 14 contrasts the validation set performance during training: adding S1 (dashed/orange) sharpens convergence and lifts mIoU by +6 to +7pp over the S2-SR-only baseline.

3.3. Transferability across regions

3.3.1. Performance on Fields of the World (FoTW) Benchmark

We compared our model to the 2-class baseline published with the FoTW benchmark (Kerner et al., 2024), which uses a U-Net with an EfficientNet-B3 backbone and was trained under identical input conditions (i.e., same number of bands and timestamps, identical splits on training/validation test folds of the FoTW dataset). Table 5 and Fig. 16 summarize the per-country results in terms of pixel-level mIoU.

Table 5: Comparison of pixel-level mIoU scores between PTAViT3D and FoTW 2-class baseline model across 25 countries. The best score per country is shown in **bold**.

Test Country	FoTW	PTAViT3D
Austria	0.77	0.87
Belgium	0.80	0.89
Brazil	–	0.60
Cambodia	0.76	0.67
Corsica	0.49	0.74
Croatia	0.76	0.85
Denmark	0.84	0.85
Estonia	0.81	0.90
Finland	0.87	0.93
France	0.82	0.84
Germany	0.80	0.86
India	–	0.59
Kenya	–	0.50
Latvia	0.84	0.91
Lithuania	0.78	0.87
Luxembourg	0.85	0.89
Netherlands	0.79	0.91
Portugal	0.29	0.56
Rwanda	–	0.57
Slovakia	0.93	0.94
Slovenia	0.69	0.85
South Africa	0.82	0.81
Spain	0.84	0.88
Sweden	0.83	0.89
Vietnam	0.67	0.73
Mean	0.76	0.80
Std	0.14	0.13
Min	0.29	0.50

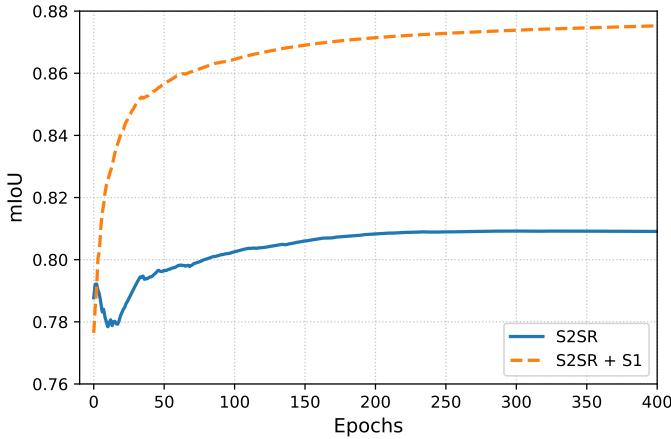


Figure 14: Performance comparison for the AI4SmallFarms dataset of models trained with a single S2 super resolution image (S2SR) vs S2SR in combination with a time series of S1 images.

Despite the fact that PTAViT3D was developed and fine-tuned within the context of the Australian cropping system, it

performs competitively or better than the FoTW baseline in the majority of evaluated countries. In 23 out of 25 test countries, PTAViT3D achieves higher mIoU than the published baseline. Notably, it consistently outperforms the baseline in diverse settings such as Finland, Slovakia, Germany, Estonia, and Sweden—regions with varied field morphologies and parcel complexities.

Overall, the summary statistics confirm that PTAViT3D offers both higher accuracy and greater robustness than the FoTW baseline. On average, PTAViT3D raises the country-level mIoU from 0.76 to 0.80, while simultaneously reducing the spread of the scores (std= 0.13 versus 0.14). Importantly, its worst-case performance is also considerably stronger: the minimum mIoU recorded across all countries is 0.50, compared with only 0.29 for the baseline. In other words, even in the most challenging settings – typically those characterised by small, highly fragmented parcels such as in Kenya or Portugal – PTAViT3D retains higher predictive quality.

While the architectural design of PTAViT3D was not specifically fine-tuned on FoTW data, its competitive performance underlines the effectiveness of its spatiotemporal encoding and attention mechanisms. These results collectively suggest that PTAViT3D generalizes well across regions and can serve as a strong baseline for future research in global field boundary segmentation.

3.3.2. Performance on the PASTIS benchmark

Table 6: Semantic-segmentation results on the PASTIS benchmark (all 19 classes, background included). We report also the results for U-TAE replicated from [Sainte Fare Garnot and Landrieu \(2021a\)](#). We used 24 random samples in Time over all time series elements. The best score is shown in **bold**.

Model	OA	mIoU	MCC
U-TAE	0.832	0.631	–
PTAViT3D (ours)	0.847	0.649	0.796

Table 7: Performance on the PASTIS dataset as a function of the number of Sentinel-2 acquisitions used (all 19 classes, background included). The best score is shown in **bold**.

Metric	16×	24×	32×	48×
Overall accuracy	0.842	0.847	0.846	0.844
mIoU	0.633	0.649	0.647	0.639
MCC	0.790	0.796	0.796	0.793

To demonstrate that PTAViT3D is not limited to field-boundary tasks, we evaluated it on the full PASTIS land-cover benchmark ([Sainte Fare Garnot and Landrieu, 2021a](#)). This dataset comprises 33–61 Sentinel-2 (S2) acquisitions per pixel; even after discarding scenes with > 90% cloud, roughly **28 %** of the remaining images still contain partial cloud cover ([Sainte Fare Garnot and Landrieu, 2021a,b](#)). We adhered to the official five-fold train/val/test split and trained with *only eight* randomly sampled acquisitions per pixel.

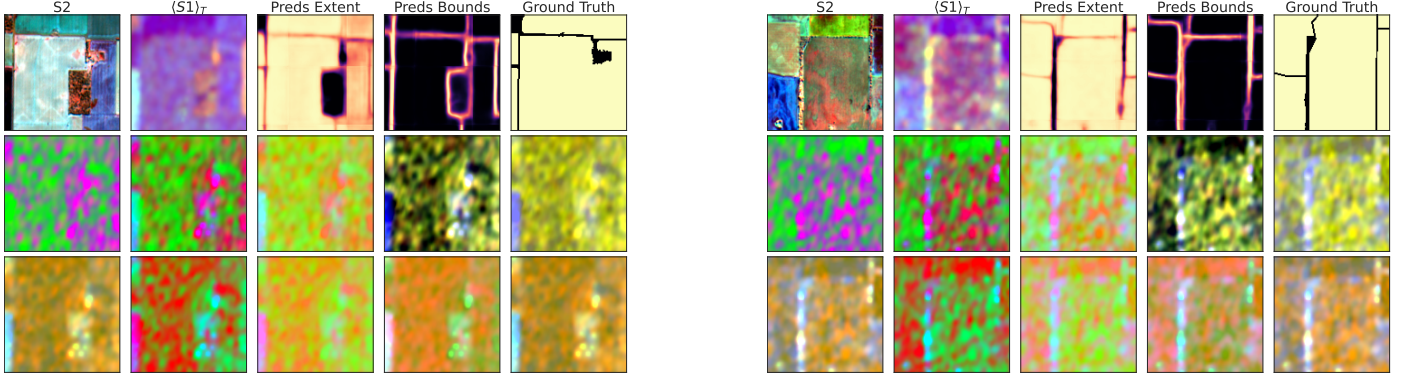


Figure 15: Illustration of the spatial-resolution enhancement achieved by PTAViT3D predictions from Sentinel-1 (S1) time series imagery. The top row shows, from left to right, the reference Sentinel-2 (S2) imagery (not used by the model, provided here solely for visual comparison), the temporal average of S1 bands (VH,VV,A), the predicted extent and boundary layers, and the Ground Truth field boundaries at S2 resolution. The next two rows visualize all possible combinations of triplets from the five available S1 bands, specifically for the last date in the time series, highlighting that no single-date or averaged snapshot matches the detailed spatial information of the temporally integrated predictions.

At inference we swept the number of snapshots, $N \in \{16, 24, 32, 48\}$ (Table 7). Accuracy peaks at $N = 24$ – **0.847** OA, **0.649** mIoU, **0.796** MCC – while varying by at most 0.01 OA if we double the time series. This plateau indicates that PTA3D extracts most of the discriminative power from just $\approx 40\%$ of the available imagery.

Using the same 24-frame protocol, Table 6 shows that PTAViT3D improves on U-TAE by +1.5 pp OA (0.847 vs 0.832) and +1.8 pp mIoU (0.649 vs 0.631) while also providing a calibrated MCC of 0.796.

The confusion matrix in Fig. 17 reveals that 14 of the 19 crop classes achieve ≥ 0.75 recall. Notable strong classes include *soft-winter wheat* (0.93 recall, 0.94 precision) and *corn* (0.95/0.95). Most errors occur among botanically similar cereals with few training samples—e.g. *mixed cereal* (0.56 IoU) and *winter triticale* (0.65 IoU).

The accompanying bar-plot (right panel, Fig. 17) highlights the extreme skew: *meadow* contributes $\approx 30\,000$ instances whereas seven classes have fewer than 2 000. Achieving high mIoU under this imbalance – without focal loss or re-weighting – shows that PTAViT3D’s patch-wise Tanimoto attention remains robust on dense, cloud-affected time series.

Overall, these findings confirm that the same architecture and hyper-parameters used for boundary delineation seamlessly transfer to multi-class crop mapping, requiring only a modest subset of the available imagery and no explicit cloud masking.

3.3.3. Smallholder rice paddies: AI4SMALLFARMS

The AI4SMALLFARMS tiles for **Cambodia** and **Vietnam** are also present in FoTW, yet the two repositories differ in both *spectral* and *temporal* content: FoTW provides *two* cloud-free Sentinel-2 (S2) composites at 10m, whereas the original AI4SMALLFARMS dataset offers only *one* S2 composite—but with access to the full reference polygon files. In addition we have acquired the Sentinel-1 (S1) time series for the cropping season that refers to the data. These two regions therefore combine (i) **persistent cloud cover** and (ii) **sub-hectare paddies**, making them

an ideal stress-test for PTAViT3D-CA with S2 and SAR fusion. Given the extra challenge of sub-hectare paddies, and since we have already modeled with original S2 resolution this dataset (FoTW), we resort to super resolution (SR) for upscaling the original S2 image. This upscaled S2 image will be fused with SAR for modeling with PTAViT3D-CA.

To accommodate the asymmetric inputs – one super-resolved S2 image versus a multi-temporal S1 stack – we remove the fusion branch of the dual encoder PTAViT3D-CA. First, each 10m Sentinel-2 composite is up-sampled offline by a factor of four with the open sourced LDSR-S2 model (Donike et al., 2025), yielding a single 2.5m S2-SR tile. The complete Sentinel-1 time series (upscaled with linear interpolation to match the spatial dimensions of S2-SR) forms the secondary branch; its features interact with those of S2 solely through Patch Tanimoto Attention 3D, avoiding any explicit feature concatenation and thus sidestepping temporal mis-alignment issues. At every encoder depth, the S2-SR feature map $f_{S_2^{SR}} \in \mathbb{R}^{B \times N \times 1 \times H \times W}$ is enriched by the attention map computed against the S1 features $f_{S_1} \in \mathbb{R}^{B \times N \times T \times H \times W}$:

$$f_{S_2^{SR}} \leftarrow f_{S_2^{SR}}(1 + \mathcal{A}(f_{S_1}, f_{S_2^{SR}}, f_{S_2^{SR}})),$$

where $\mathcal{A}(\cdot)$ denotes PTA3D (Eq. (9)). We note that the S2-SR image features are used as key-value pairs. Given that \mathcal{A} contracts the time dimension of the query features f_{S_1} , during the query-key interaction, its output is dimensionally compatible with $f_{S_2^{SR}}$ (see Fig. 7). In practice this design lets the cloud-immune temporal cues in S1 refine the high-resolution spatial detail recovered from S2-SR.

Beginning with the native 10m Sentinel-2 composites, we first apply LDSR-S2 to obtain a $4\times$ super-resolved image at 2.5m. The ground-truth parcel polygons are rasterised on this high-resolution grid, and we again construct the extent, bounds and distance transform (per parcel). We then feed the resulting S2-SR image, together with the full Sentinel-1 time series, into the joint S2-SR& S1 variant of PTAViT3D-CA, whose multitask heads output *extent*, a distance-transform map and aux-

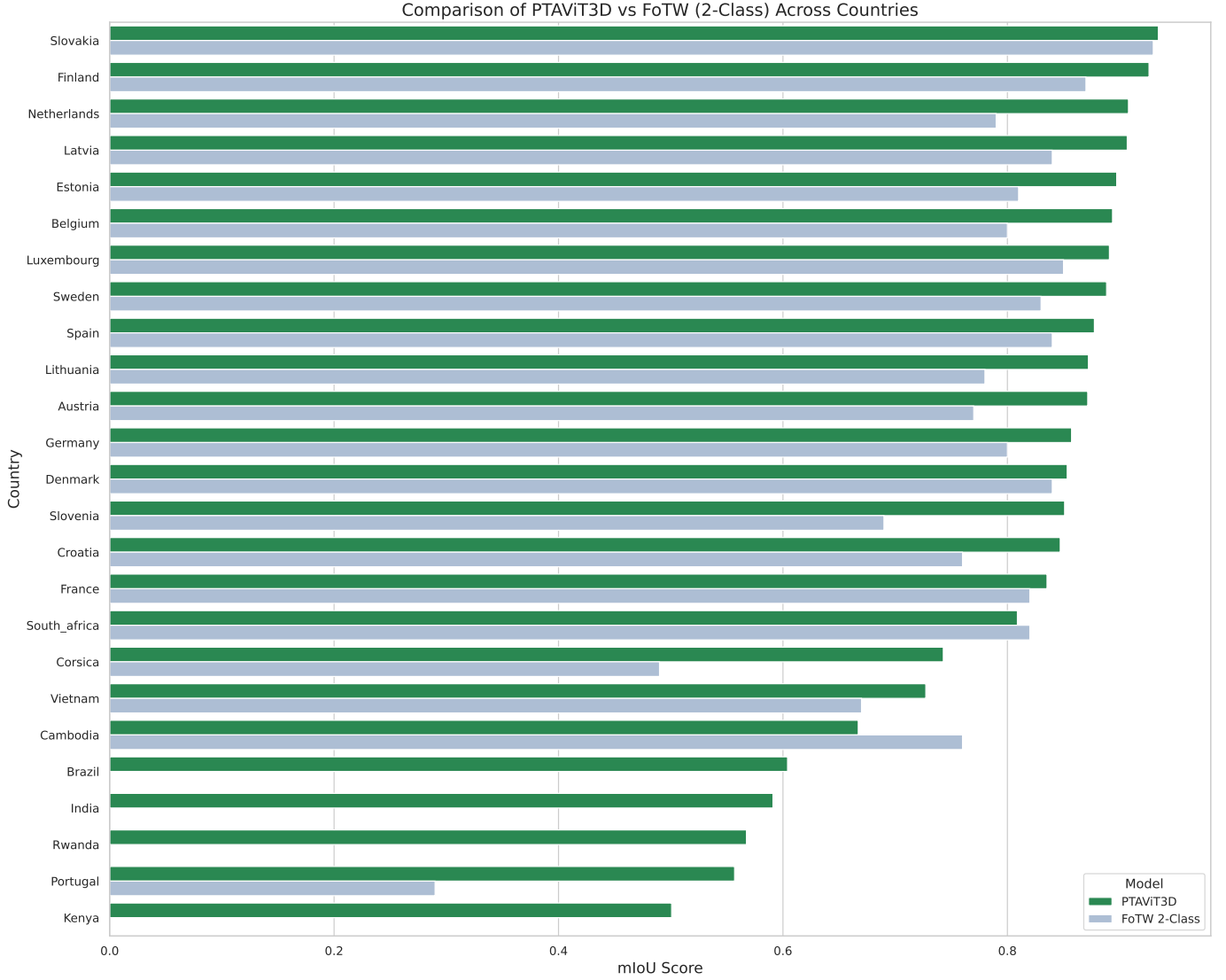


Figure 16: Performance on FoTW in comparison with Baseline for each country.

iliary edge logits. We also train a pure PTAViT (2D) model with the S2-SR input for comparison with the fused model S2-SR& S1.

During inference, the predictions logits are used in two ways, either in the predicted 2.5m resolution or they are down-sampled to the original 10m resolution—using the mean for the *extent* channel and the maximum for the *boundary* channel—so that predictions remain directly comparable with the pixel-level evaluation metrics.

Given the clear superiority of S2-SR& S1 model over the pure S2-SR one (Fig. 14), we proceed in test set evaluation only with the former (Table 8). Starting the comparison with the FoTW trained model, the S2-SR& S1 model outperforms all baselines and our previous model with IoU 92.5% for Cambodia (+16% over baseline, +25% over our best model trained on FoTW data) and 79.9% for Vietnam (+7% over our best model trained on FoTW, +13% over the baseline). The corresponding

boundary F1 score (10m resolution) of 51.6% improves on the baseline (39%) reported by Persello et al. (2023) by $\sim +11\%$. For the case of the 2.5m resolution (super resolution imagery) the Extent metrics remain all high, however the Boundary metrics (corresponding to a single pixel thickness) fall to low values, much lower than the corresponding 0.5m Google Maps (GM) results reported from Persello et al. (2023). However, the PoLiS distance remains high both in 10m and 2.5m resolution, surpassing the Persello et al. (2023) baseline, suggesting that the problem with the low score in boundary pixels is mainly owed to our model missing the 1 pixel width of boundaries for the 2.5m case. Indeed during training the reference boundaries are deliberately rasterised with a width of three pixels to stabilise optimisation. When these wide predictions are morphologically thinned back to a one-pixel skeleton for evaluation, any localisation error larger than half a pixel propagates outward, effectively inflating the positional bias at the higher

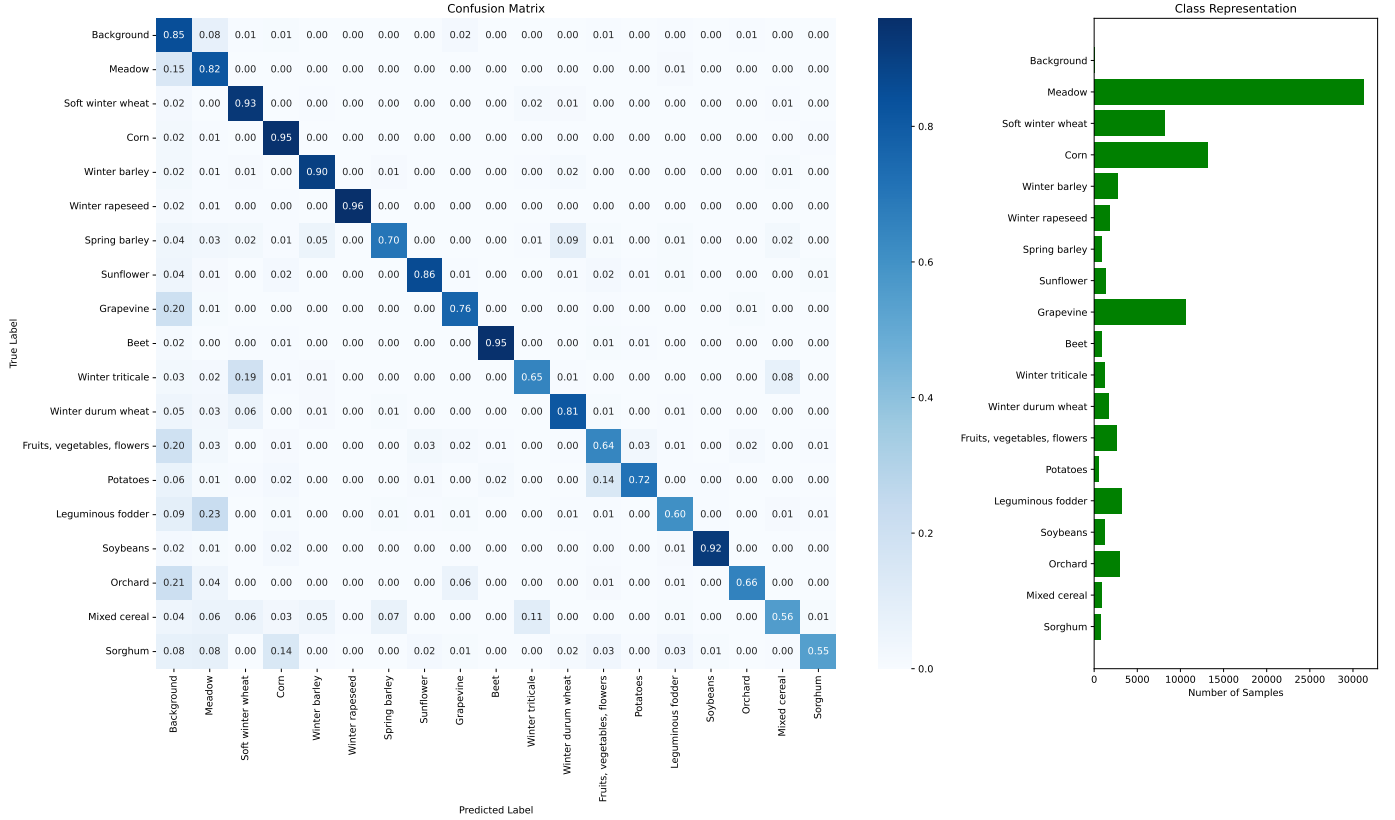


Figure 17: Performance over 19 classes on Pastis dataset using randomly sampled 24 instances of S2 time images.

resolution. The fact that parcel *area* metrics remain excellent at 2.5m supports the view that the model is operating in an error-tolerant regime with respect to boundary thickness, rather than misclassifying large regions.

For the case of the S2-SR& S1 model, in Fig. 18 we present qualitative results for the two test tiles of Cambodia 12 (top) and Vietnam 27 (bottom). From left to right we plot for each row: the Original resolution S2 (10m) image, the refined extent masks that our model predicts, the ground truth at super resolution of 2.5m of polygons and finally, the agreement between predicted polygons and ground truth. Fig. 19 is the same, however with zoomed in regions so interested readers can evaluate qualitatively the boundaries results.

Unlike the Australian case—where S1 merely matched S2 performance—the Cambodia/Vietnam paddies gain a ≈ 0.06 – 0.07 mIoU boost when S1 is introduced. The SAR signal provides cloud-proof temporal cues that complement the spatial detail recovered by SR S2, yielding the best of both worlds.

3.4. PTAiT3D continental scale application: the ePaddocks National product of Australia

In this section we provide a detailed roadmap on applying the PTAiT3D algorithm at continental scale. We also utilize the results to compare with previous established baselines (Waldner and Diakogiannis, 2020; Waldner et al., 2021). To

construct the National Product (ePaddocks) of Australia for 2023, we followed these steps:

1. We initially pretrained the PTAiT3D on six tiles from Australia using 2019 data, the same data used for creating ePaddocks 2019 (Figure 2).
2. We then sourced new imagery for the same date range (2019) using OpenDataCube (ODC⁴) and fine-tuned the algorithm on these new images, ensuring they had $\leq 10\%$ cloud cover. This mimicked the expected conditions during inference, as opposed to the clear rasters used for initial pretraining. It also enriches the algorithm by exposing it to greater variability of input imagery during training.
3. Inference for the year 2023 was performed across 293 tiles, as shown in Figure 2. This process created raster products that combined field extent, boundaries, and distance transform.
4. To transition from semantic segmentation to instance segmentation, we post-processed the data (Section 3.4.1) using set operations, thresholding, and extracted polygons with the rasterio (Gillies et al., 2013–) features module.

⁴<https://www.opendatacube.org/>

Table 8: Evaluation on the AI4SMALLFARMS *test* split. Top block in each region: **pixel-level** precision (P), recall (R), F_1 and IoU for field extent and boundary. Bottom block: **polygon-level** mean PoLiS, (symmetric) Hausdorff distance and mean surface distance (MSD). Best score in each sub-category, where baselines exist for comparison, is in **bold**.

Region / Mask		P	R	F_1	IoU
Global	Extent (2.5m-ours)	0.933	0.874	0.902	0.822
	Extent (10m-ours)	0.935	0.933	0.934	0.876
	Boundary (2.5m-ours)	0.193	0.135	0.159	0.086
	Boundary (10m-ours)	0.567	0.480	0.520	0.351
	Boundary (10m-Persello et al. (2023))	0.480	0.330	0.390	–
	Boundary (0.5m-Persello et al. (2023))	0.47	0.52	0.49	–
	PoLiS (2.5m-ours)	14.35m			
	PoLiS (10m-ours)	15.06m			
	PoLiS (10m-Persello et al. (2023))	26.7m			
	PoLiS (0.5m-Persello et al. (2023))	20.3m			
Cambodia	Extent (2.5m-ours)	0.962	0.894	0.926	0.863
	Extent (10m-ours)	0.962	0.959	0.961	0.925
	Extent (10m-Kerner et al. (2024))	–	–	–	0.760
	Boundary (2.5m-ours)	0.187	0.143	0.162	0.088
	Boundary (10m-ours)	0.566	0.502	0.532	0.362
	PoLiS (2.5m-ours)	12.01m			
	PoLiS (10m-ours)	12.73m			
Vietnam	Extent (2.5m-ours)	0.884	0.839	0.861	0.756
	Extent (10m-ours)	0.888	0.888	0.888	0.799
	Extent (10m-Kerner et al. (2024))	–	–	–	0.670
	Boundary (2.5m-ours)	0.204	0.123	0.154	0.083
	Boundary (10m-ours)	0.569	0.450	0.503	0.336
	PoLiS (2.5m-ours)	19.54m			
	PoLiS (10m-ours)	20.25m			

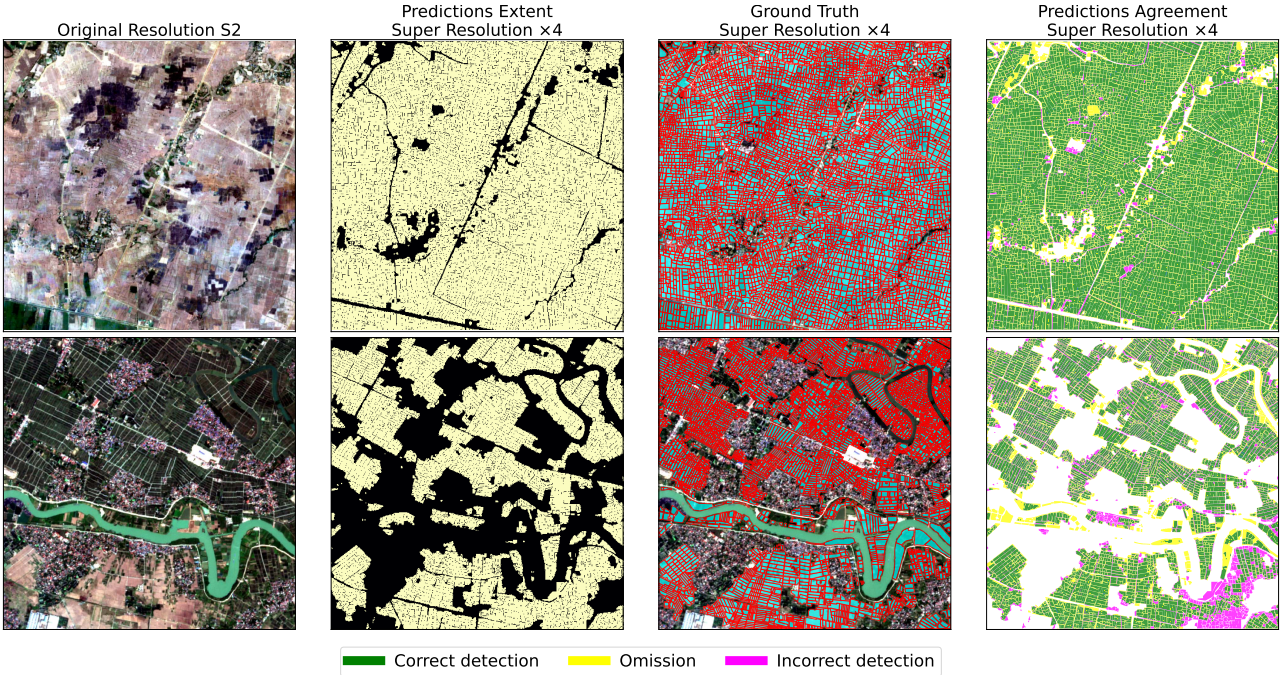


Figure 18: Sample performance from the test set on tiles Cambodia 12 (top) and Vietnam 27 (bottom).

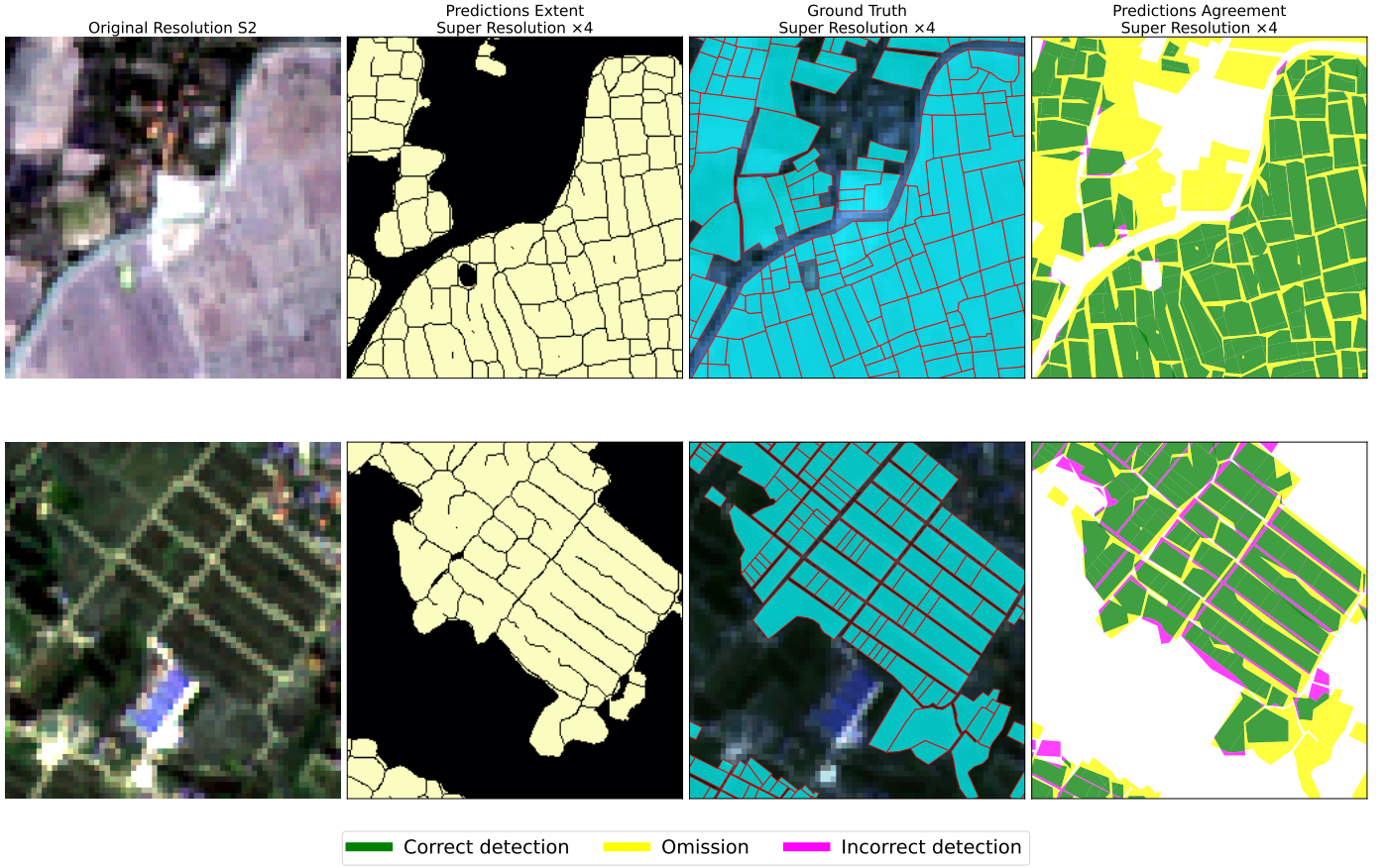


Figure 19: As Fig. 18, zoomed in random regions on tiles Cambodia 12 (top) and Vietnam 27 (bottom).

5. Further post-processing was done to remove inference results smaller than 100m^2 and to simplify polygons with a 10m (1 pixel) tolerance.
6. The test set was validated on 67 small raster patches, each approximately 100km^2 , which were manually annotated by our internal CSIRO team.

Qualitative indicative performance on the test set of 2023 can be seen in Figure 20, where we visualize from left to right, a single date of S2 imagery, the field pseudo-probability, the predicted polygon fields, the ground truth fields and the agreement between them.

3.4.1. Post processing: from raster predictions to shapefiles

Let e and b represent the predicted extent and boundaries layers, respectively. These layers capture essential information for instance segmentation, with various algorithms transitioning from semantic to instance segmentation (e.g., watershed segmentation (Waldner and Diakogiannis, 2020), hierarchical segmentation (Waldner et al., 2021)). Here, we present a practical and easy-to-implement approach that utilizes the predicted extent and boundary layers.

The first step involves refining the extent layer using two distinct thresholds: one for the extent, t_e , and another for the

boundaries, t_b . Initially, the predicted boundaries, b , are thresholded with t_b and undergo morphological thinning to reduce their thickness, followed by a dilation to ensure a single-pixel width. This thinned boundary layer provides a fine segmentation that ensures clear separation between neighboring fields.

Next, the extent layer, e , is combined with the inverted thinned boundaries, $1 - b$, to produce a refined mask. This combination is achieved by taking the fuzzy set intersection of e and $1 - b$, realized by multiplying the extent with the complement of the boundaries, $e \cap \bar{b}$, and then thresholding the result based on the extent threshold, t_e . This process yields a binary mask that highlights the extents of the fields without the influence of boundaries, ensuring accurate delineation.

We then utilize the rasterio library (Gillies et al., 2013–) to convert this refined raster mask into polygon shapefiles. The refined extent mask is passed to the rasterio features.shapes function, which identifies contiguous regions in the binary mask and converts them into geometric shapes. These shapes are then converted into a GeoDataFrame, maintaining the correct spatial reference system (CRS) from the input metadata. The resulting GeoDataFrame can be saved as a shapefile for further analysis or visualization (Listing 2). This approach leverages the strengths of the predicted extent and boundary layers to

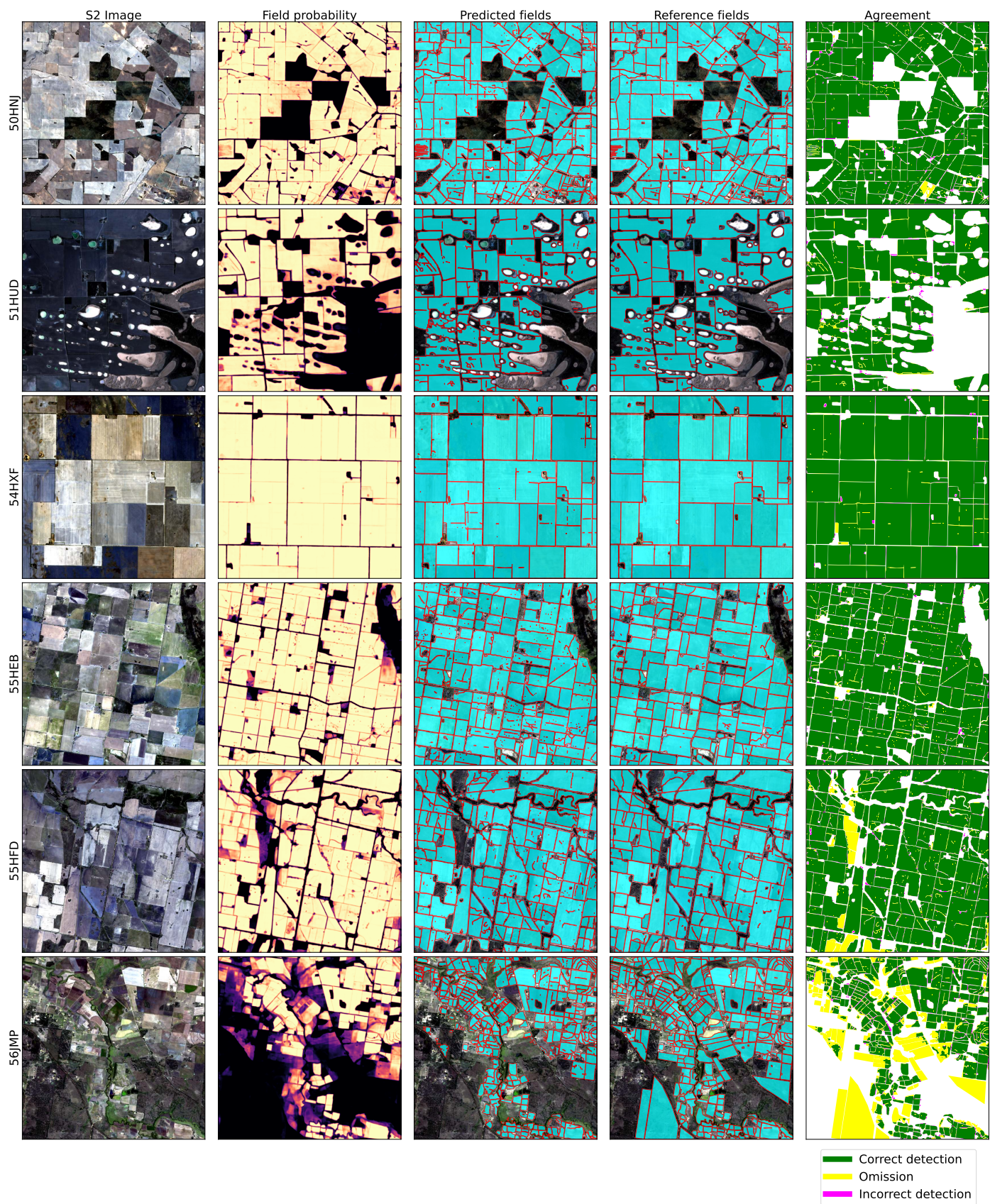


Figure 20: Example of Instance Segmentation for the field boundaries in five test sites (year 2023). In the agreement column, white space indicates agreement in background.

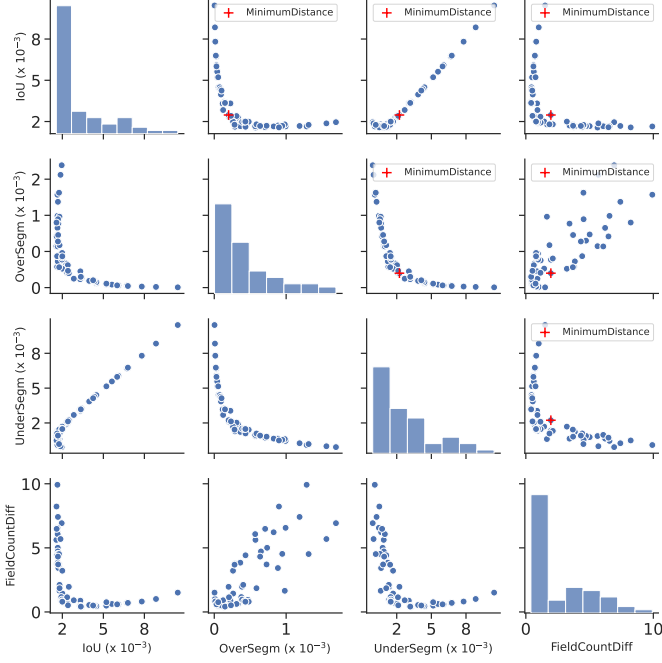


Figure 21: Pareto front of the multiobjective optimization for the estimation of instance segmentation hyperparameters.

accurately delineate field boundaries, providing a straightforward and efficient method for converting raster predictions into vector formats suitable for geospatial applications. The performance of this approach depends on the choice of the extent and boundary thresholds used, that we evaluate using a multiobjective optimization routine.

In Figure 21 we show the pareto front for the following metrics, *IoU*, *FDR* (ovesegmentation), *FOR* (undersegmentation) and the difference in counts of total number of fields. The optimum choice was selected for the point of the pareto front closest to the origin (0) of the coordinate system, that represents the ideal minimum. The optimization was performed with the library *optuna* (Akiba et al., 2019) and the best choice of thresholds was found to be $t_b \approx 0.2$ and $t_e \approx 0.4$.

3.4.2. ePaddocks Test Set Evaluation

The ePaddocks test set evaluation was conducted using 67 test tiles, each approximately 100km², across the cropping zones of Australia (Section 2.1.1). The evaluation focused on two main aspects: segmentation performance using raster data and polygon boundaries matching performance.

Segmentation Performance (Raster Data). The segmentation performance was assessed using raster data with the following metrics (Figure 22):

Intersection over Union (IoU): The mean IoU was 0.804 ± 0.194 , indicating a high degree of overlap between the predicted and actual field boundaries.

False Omission Rate (FOR): The mean FOR was 0.283 ± 0.194 , reflecting the extent of under-segmentation in the predictions. The increased omission rate primarily stems from the

1-pixel buffer in the boundaries we evaluated based on ground truth. This buffer leads to more conservative field boundaries (Fig. 20), which is a result of the raster-to-polygon strategy we followed. Although this strategy has the drawback of more conservative boundaries, it also ensures that boundary fields do not intersect.

False Discovery Rate (FDR): The mean FDR was 0.011 ± 0.011 , showcasing an extremely low rate of false positives. This indicates that the model rarely identified non-field areas as fields, resulting in excellent performance for false discovery.

These metrics demonstrate that the segmentation model performs well, with high accuracy in identifying field boundaries and a minimal number of false positives. The conservative boundaries strategy leads to higher omission rates but prevents overlapping boundaries.

Polygon Matching Performance. The performance of the polygon matching was evaluated for polygons with an IoU of at least 0.001 using the following metrics (Figure 23):

Intersection over Union (IoU): The mean IoU was 0.893 ± 0.221 , indicating a higher degree of overlap when compared to the raster evaluation. The difference between the IoU value estimated from segmentation predictions and polygons (0.893 vs 0.804 for rasters) is due to two main reasons: (a) the IoU for polygons is computed as the average IoU across individual polygons rather than across tiles, resulting in a different computation as it is per object; (b) there is a small selection bias, as matches with an IoU smaller than 10^{-3} were excluded to ensure meaningful matches.

Hausdorff Distance: The mean Hausdorff Distance was 224.998 ± 192.163 , measuring the greatest distance between the predicted and actual field boundaries. This large variance reflects the variability in the complexity of field shapes across the test set.

Mean Surface Distance (MSD): The mean MSD was 39.076 ± 38.706 , which provides an average measure of the distance between the surfaces of the predicted and actual polygons. This is approximately 4 pixels, or 40m on average.

These metrics indicate that the model’s polygon predictions align closely with the actual field boundaries, although the Hausdorff Distance suggests some variability due to the diverse shapes of the fields.

Figure 24 (see also Figure 20) illustrates the agreement per field example with representative boundary metrics. These examples underscore the model’s ability to accurately delineate field boundaries while minimizing errors, as evidenced by the low FDR.

The ePaddocks test set evaluation confirms the robustness and accuracy of the proposed model in detecting field boundaries from Sentinel-2 time series imagery. The results demonstrate that the model performs effectively in both raster-based segmentation and polygon-based boundary delineation, making it a reliable tool for field boundary mapping in diverse agricultural landscapes. The conservative boundary delineation strategy results in higher omission rates but ensures non-intersecting fields, which is a significant advantage for practical applications.

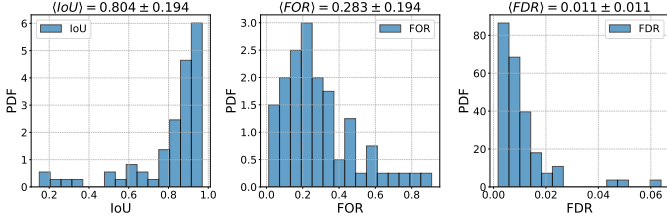


Figure 22: Segmentation performance on the Test set, model trained on S2 time series. These metric are evaluated from raster data, not polygons.

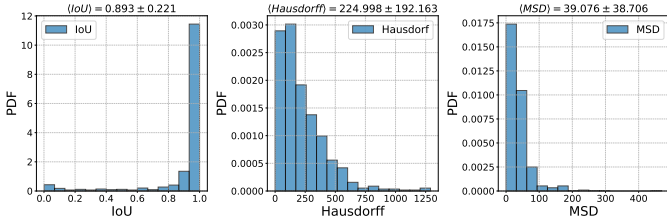


Figure 23: Segmentation performance on the Test set, model trained on S2 time series. These metric are evaluated from Polygons not rasters.

4. Discussion

This study introduces and comprehensively evaluates the PTAViT3D and PTAViT3D-CA models for robust field boundary delineation using Sentinel-1 (S1) and Sentinel-2 (S2) satellite image time series (SITS). Our approach specifically targets scenarios with sparse and dense cloud contamination, demonstrating remarkable resilience and performance consistency under challenging atmospheric conditions. A key finding from our experiments is that PTAViT3D using S1 imagery achieves a spatial resolution comparable to S2-based predictions, proving highly advantageous for cloud-prone regions. This capability significantly advances previous approaches (e.g., (Waldner and Diakogiannis, 2020; Waldner et al., 2021)), which required cloud-free or minimally clouded imagery and manual intervention for data preparation.

The integration of temporal data via our novel 3D Vision Transformer architecture marks a substantial advancement. By capturing inherent spatio-temporal correlations explicitly, the PTAViT3D architecture significantly improves the reliability of field boundary predictions without resorting to traditional cloud masking or pixel removal methods. This methodological advancement streamlines workflows for digital agricultural services and enhances data integrity, potentially benefiting downstream applications such as crop yield estimation and water quality forecasting.

Our extensive evaluation included not only Australia’s ePad-docks dataset but also globally diverse benchmarks such as Fields of the World (FoTW), PASTIS, and AI4SmallFarms datasets. These evaluations demonstrated strong generalizability and transferability of our approach. On the FoTW dataset, our model consistently outperformed existing benchmarks, highlighting its adaptability across different global agricultural landscapes. The PASTIS dataset, which represents varying cloud conditions and

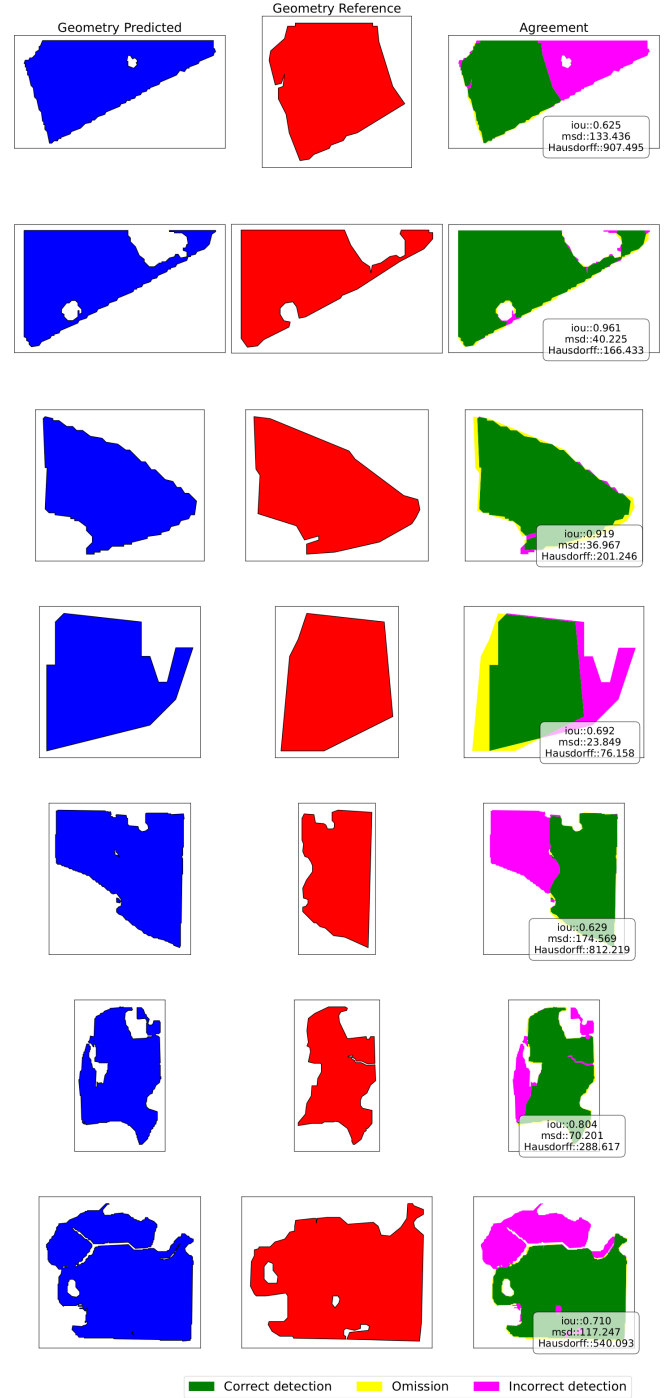


Figure 24: Agreement per field example with representative boundary metrics

multiple crop types, further illustrated the robustness of PTAViT3D, achieving improvements over established models like U-TAE (Sainte Fare Garnot and Landrieu, 2021a), with a fraction of the available time series of S2 observations. Notably, PTAViT3D effectively managed severe class imbalances and partial cloud coverage without specialized re-weighting or masking, underscoring its practicality and versatility.

Moreover, the AI4SmallFarms dataset highlighted the benefits of combining S1 with super-resolved S2 imagery, particularly in challenging smallholder environments characterized by fragmented landscapes and persistent cloud cover. The inclusion of S1 data notably improved performance and convergence speed, reinforcing the practical value of multimodal satellite imagery fusion for precise field boundary delineation in cloud-affected areas.

The development of the 2023 ePaddocks product exemplifies the scalability of our model, demonstrating its capability for operational deployment at continental scales. It serves as a comprehensive roadmap illustrating best practices and detailed procedures necessary for successful implementation at such scales. Furthermore, the ePaddocks 2023 dataset facilitates rigorous comparisons with established baselines such as those presented by Waldner and Diakogiannis (2020); Waldner et al. (2021), enhancing transparency and reproducibility in large-scale remote sensing applications.

Several avenues exist to further enhance the performance and applicability of our methodology. These include transitioning from field boundary delineation to crop-type classification, developing end-to-end polygon inference methods to replace post-processing steps, and incorporating geographical encoding, potentially through methodologies like SatCLIP (Klemmer et al., 2023). Additionally, our findings highlight the promising potential of automated super-resolution methods combined with field boundary delineation tasks. Integrating super-resolution approaches systematically could further refine spatial detail and overall model accuracy, particularly in fragmented agricultural landscapes.

5. Conclusion

In this study, we presented PTAViT3D and its cross-attention extension PTAViT3D-CA, novel deep learning architectures explicitly designed for robust field boundary delineation using Sentinel-1 and Sentinel-2 satellite imagery time series. Our approaches address critical limitations of traditional remote sensing methods, notably those associated with cloud contamination and extensive manual preprocessing requirements. Through comprehensive evaluations using Australia’s ePaddocks dataset and publicly available benchmarks (FoTW, PASTIS, AI4SmallFarms), our models consistently demonstrated superior or competitive performance, remarkable cloud tolerance, and exceptional generalizability across diverse agricultural landscapes.

The PTAViT3D framework significantly simplifies the operational workflow, reducing computational overhead by avoiding cloud masking and manual image selection. Our results underscore the substantial practical value of integrating both SAR (Sentinel-1) and optical (Sentinel-2) satellite data, offering robust alternatives under varying cloud conditions. By effectively capturing spatio-temporal relationships, our approach ensures reliable predictions, enhances data integrity, and ultimately supports more informed decision-making in agricultural management.

Given these contributions, PTAViT3D represents a meaningful advancement toward automated, scalable, and robust agri-

cultural boundary delineation solutions. It particularly excels in global applicability, reproducibility through open-source code, and the provision of detailed guidelines for large-scale deployment, as demonstrated by the ePaddocks 2023 continental-scale implementation. Future work will build on these foundations to further refine model capabilities, particularly in polygon-level inference, geographical feature integration, automated super-resolution techniques, and expanded applications in crop-type classification and other environmental monitoring tasks.

Acknowledgments

This project was supported by resources and expertise provided by CSIRO IMT Scientific Computing.

References

- ABARES, 2016. The Australian land use and management classification version 8. URL: <https://www.agriculture.gov.au/abares/aclump/land-use/alum-classification>.
- Akiba, T., Sano, S., Yanase, T., Ohta, T., Koyama, M., 2019. Optuna: A next-generation hyperparameter optimization framework, in: Proceedings of the 25th ACM SIGKDD International Conference on Knowledge Discovery & Data Mining, Association for Computing Machinery, New York, NY, USA. p. 2623–2631. URL: <https://doi.org/10.1145/3292500.3330701>, doi:10.1145/3292500.3330701.
- Aung, H.L., UzKent, B., Burke, M., Lobell, D., Ermon, S., 2020. Farm parcel delineation using spatio-temporal convolutional networks, in: 2020 IEEE/CVF Conference on Computer Vision and Pattern Recognition Workshops (CVPRW), p. 340–349. doi:10.1109/CVPRW50498.2020.00046.
- Avbelj, J., Müller, R., Bamler, R., 2015. A metric for polygon comparison and building extraction evaluation. IEEE Geoscience and Remote Sensing Letters 12, 170–174. doi:10.1109/LGRS.2014.2330695.
- Benjamini, Y., Hochberg, Y., 2018. Controlling the false discovery rate: A practical and powerful approach to multiple testing. Journal of the Royal Statistical Society: Series B (Methodological) 57, 289–300. URL: <https://doi.org/10.1111/j.2517-6161.1995.tb02031.x>, doi:10.1111/j.2517-6161.1995.tb02031.x.
- Blaes, X., Vanhale, L., Defourny, P., 2005. Efficiency of crop identification based on optical and SAR image time series. Remote Sensing of Environment 96, 352–365. doi:10.1016/j.rse.2005.03.010.
- Buslaev, A., Iglovikov, V.I., Khvedchenya, E., Parinov, A., Druzhinin, M., Kalinin, A.A., 2020. Albumentations: Fast and flexible image augmentations. Information 11. URL: <https://www.mdpi.com/2078-2489/11/2/125>, doi:10.3390/info11020125.
- Cai, Z., Hu, Q., Zhang, X., Yang, J., Wei, H., Wang, J., Zeng, Y., Yin, G., Li, W., You, L., Xu, B., Shi, Z., 2023. Improving agricultural field parcel delineation with a dual branch spatiotemporal fusion network by integrating multimodal satellite data. ISPRS Journal of Photogrammetry and Remote Sensing 205, 34–49. URL: <https://www.sciencedirect.com/science/article/pii/S0924271623002630>, doi:10.1016/j.isprsjprs.2023.09.021.
- Cloude, S., 2007. The dual polarization entropy/alpha decomposition: A polar case study, in: Lacoste, H., Ouwehand, L. (Eds.), Science and Applications of SAR Polarimetry and Polarimetric Interferometry, p. 2.
- Cloude, S., Pottier, E., 1997. An entropy based classification scheme for land applications of polarimetric SAR. IEEE Transactions on Geoscience and Remote Sensing 35, 68–78.
- d’Andrimont, R., Claverie, M., Kempeneers, P., Muraro, D., Yordanov, M., Peressutti, D., Batič, M., Waldner, F., 2023. Ai4boundaries: an open ai-ready dataset to map field boundaries with sentinel-2 and aerial photography. Earth System Science Data 15, 317–329. URL: <https://essd.copernicus.org/articles/15/317/2023/>, doi:10.5194/essd-15-317-2023.
- Diakogiannis, F.I., Furby, S., Caccetta, P., Wu, X., Ibata, R., Hlinka, O., Taylor, J., 2024. Ssg2: A new modeling paradigm for semantic segmentation. ISPRS Journal of Photogrammetry and Remote Sensing 215, 44–61. URL: <https://www.sciencedirect.com/science/article/pii/S0924271624002491>, doi:10.1016/j.isprsjprs.2024.06.011.

- Diakogiannis, F.I., Waldner, F., Caccetta, P., 2021. Looking for change? roll the dice and demand attention. *Remote Sensing* 13. URL: <https://www.mdpi.com/2072-4292/13/18/3707>, doi:10.3390/rs13183707.
- Diakogiannis, F.I., Waldner, F., Caccetta, P., Wu, C., 2020. Resunet-a: A deep learning framework for semantic segmentation of remotely sensed data. *ISPRS Journal of Photogrammetry and Remote Sensing* 162, 94–114. URL: <http://www.sciencedirect.com/science/article/pii/S0924271620300149>, doi:10.1016/j.isprsjprs.2020.01.013.
- Donike, S., Aybar, C., Gómez-Chova, L., Kalaitzis, F., 2025. Trustworthy super-resolution of multispectral sentinel-2 imagery with latent diffusion. *IEEE Journal of Selected Topics in Applied Earth Observations and Remote Sensing* 18, 6940–6952. doi:10.1109/JSTARS.2025.3542220.
- Gillies, S., et al., 2013–. Rasterio: geospatial raster i/o for Python programmers. URL: <https://github.com/rasterio/rasterio>.
- Gorodkin, J., 2004. Comparing two k-category assignments by a k-category correlation coefficient. *Computational Biology and Chemistry* 28, 367–374. URL: <https://www.sciencedirect.com/science/article/pii/S1476927104000799>, doi:10.1016/j.compbiolchem.2004.09.006.
- Graesser, J., Ramankutty, N., 2017. Detection of cropland field parcels from landsat imagery. *Remote Sensing of Environment* 201, 165–180. URL: <https://www.sciencedirect.com/science/article/pii/S0034425717303930>, doi:10.1016/j.rse.2017.08.027.
- Haghighi, S., Jasemi, M., Hessabi, S., Zolanvari, A., 2018. PyCM: Multiclass confusion matrix library in python. *Journal of Open Source Software* 3, 729. URL: <https://doi.org/10.21105/joss.00729>, doi:10.21105/joss.00729.
- Kerner, H., Chaudhari, S., Ghosh, A., Robinson, C., Ahmad, A., Choi, E., Jacobs, N., Holmes, C., Mohr, M., Dodhia, R., et al., 2024. Fields of the world: A machine learning benchmark dataset for global agricultural field boundary segmentation. *arXiv preprint arXiv:2409.16252*.
- Klemmer, K., Rolf, E., Robinson, C., Mackey, L., Rußwurm, M., 2023. Satclip: Global, general-purpose location embeddings with satellite imagery. *arXiv preprint arXiv:2311.17179*.
- Li, Z., Shen, H., Weng, Q., Zhang, Y., Dou, P., Zhang, L., 2022. Cloud and cloud shadow detection for optical satellite imagery: Features, algorithms, validation, and prospects. *ISPRS Journal of Photogrammetry and Remote Sensing* 188, 89–108. URL: <https://www.sciencedirect.com/science/article/pii/S0924271622000934>, doi:10.1016/j.isprsjprs.2022.03.020.
- Liu, L., Jiang, H., He, P., Chen, W., Liu, X., Gao, J., Han, J., 2020. On the variance of the adaptive learning rate and beyond, in: *International Conference on Learning Representations*. URL: <https://openreview.net/forum?id=rkgz2aEKDr>.
- Loshchilov, I., Hutter, F., 2017. Sgdr: Stochastic gradient descent with warm restarts, in: *Proceedings of the 5th International Conference on Learning Representations (ICLR)*. URL: <https://openreview.net/forum?id=Skq89Scxx>.
- Mascolo, L., Lopez-Sanchez, J.M., Cloude, S., 2022. Thermal noise removal from polarimetric sentinel-1 data. *IEEE Geoscience and Remote Sensing Letters* 19, 1–5. URL: <https://doi.org/10.1109/lgrs.2021.3050921>, doi:10.1109/lgrs.2021.3050921.
- Matthews, B., 1975. Comparison of the predicted and observed secondary structure of t4 phage lysozyme. *Biochimica et Biophysica Acta (BBA) - Protein Structure* 405, 442–451. URL: <http://www.sciencedirect.com/science/article/pii/0005279575901099>, doi:10.1016/0005-2795(75)90109-9.
- Matton, N., Canto, G.S., Waldner, F., Valero, S., Morin, D., Inglada, J., Arias, M., Bontemps, S., Koetz, B., Defourny, P., 2015. An automated method for annual cropland mapping along the season for various globally-distributed agrosystems using high spatial and temporal resolution time series. *Remote Sensing* 7, 13208–13232. URL: <https://www.mdpi.com/2072-4292/7/10/13208>, doi:10.3390/rs71013208.
- Michel, J., Youssefi, D., Grizonnet, M., 2015. Stable mean-shift algorithm and its application to the segmentation of arbitrarily large remote sensing images. *IEEE Transactions on Geoscience and Remote Sensing* 53, 952–964. doi:10.1109/TGRS.2014.2330857.
- Mueller, M., Segl, K., Kaufmann, H., 2004. Edge- and region-based segmentation technique for the extraction of large, man-made objects in high-resolution satellite imagery. *Pattern Recognition* 37, 1619–1628. URL: <https://www.sciencedirect.com/science/article/pii/S0031320304000548>, doi:10.1016/j.patcog.2004.03.001.
- Open Data Cube, Accessed: 2023. An open source geospatial data management & analysis platform. Open Data Cube Website. URL: <https://www.opendatacube.org/>, accessed on: yyyy-mm-dd.
- Persello, C., Grift, J., Fan, X., Paris, C., Hänsch, R., Koeva, M., Nelson, A., 2023. Ai4smallfarms: A dataset for crop field delineation in southeast asian smallholder farms. *IEEE Geoscience and Remote Sensing Letters* 20, 1–5. doi:10.1109/LGRS.2023.3323095.
- Persello, C., Tolpekin, V., Bergado, J., de By, R., 2019. Delineation of agricultural fields in smallholder farms from satellite images using fully convolutional networks and combinatorial grouping. *Remote Sensing of Environment* 231, 111253. URL: <https://www.sciencedirect.com/science/article/pii/S003442571930272X>, doi:10.1016/j.rse.2019.111253.
- Powers, D., 2011. Evaluation: From precision, recall and f-measure to roc, informedness, markedness & correlation. *Journal of Machine Learning Technologies* 2, 37–63.
- Sainte Fare Garnot, V., Landrieu, L., 2021a. Panoptic segmentation of satellite image time series with convolutional temporal attention networks. *ICCV*.
- Sainte Fare Garnot, V., Landrieu, L., 2021b. Panoptic segmentation of satellite image time series with convolutional temporal attention networks. *ICCV*.
- Snoek, J., Larochelle, H., Adams, R.P., 2012. Practical bayesian optimization of machine learning algorithms, in: Pereira, F., Burges, C., Bottou, L., Weinberger, K. (Eds.), *Advances in Neural Information Processing Systems*, Curran Associates, Inc. URL: https://proceedings.neurips.cc/paper_files/paper/2012/file/05311655a15b75fab86956663e1819cd-Paper.pdf.
- Solano-Correa, Y.T., Meshkini, K., Bovolo, F., Bruzzone, L., 2022. Automatic large-scale precise mapping and monitoring of agricultural fields at country level with sentinel-2 sats. *IEEE Journal of Selected Topics in Applied Earth Observations and Remote Sensing* 15, 3131–3145. doi:10.1109/JSTARS.2022.3164547.
- Tetteh, G.O., Schwieder, M., Erasm, S., Conrad, C., Gocht, A., 2023. Comparison of an optimised multiresolution segmentation approach with deep neural networks for delineating agricultural fields from sentinel-2 images. *PFG – Journal of Photogrammetry, Remote Sensing and Geoinformation Science* 91, 295–312. URL: <https://doi.org/10.1007/s41064-023-00247-x>, doi:10.1007/s41064-023-00247-x.
- Tian, C., Chen, X., Chen, J., Cao, R., Liu, S., 2024. Fieldseg-da2.0: Further enhancing the spatiotemporal transferability of an individual arable field (iaf) extraction network using multisource remote sensing and land cover data. *Computers and Electronics in Agriculture* 222, 109050. URL: <https://www.sciencedirect.com/science/article/pii/S0168169924004411>, doi:10.1016/j.compag.2024.109050.
- Ticehurst, C., Zhou, Z.S., Lehmann, E., Yuan, F., Thankappan, M., Rosenqvist, A., Lewis, B., Paget, M., 2019. Building a sar-enabled data cube capability in australia using sar analysis ready data. *Data* 4. URL: <https://www.mdpi.com/2306-5729/4/3/100>, doi:10.3390/data4030100.
- Tu, Z., Talebi, H., Zhang, H., Yang, F., Milanfar, P., Bovik, A., Li, Y., 2022. Maxvit: Multi-axis vision transformer. *ECCV*.
- Turker, M., Kok, E.H., 2013. Field-based sub-boundary extraction from remote sensing imagery using perceptual grouping. *ISPRS Journal of Photogrammetry and Remote Sensing* 79, 106–121. URL: <https://www.sciencedirect.com/science/article/pii/S092427161300052X>, doi:10.1016/j.isprsjprs.2013.02.009.
- Waldner, F., Diakogiannis, F.I., 2020. Deep learning on edge: Extracting field boundaries from satellite images with a convolutional neural network. *Remote Sensing of Environment* 245, 111741. URL: <http://www.sciencedirect.com/science/article/pii/S0034425720301115>, doi:10.1016/j.rse.2020.111741.
- Waldner, F., Diakogiannis, F.I., Batchelor, K., Ciccosto-Camp, M., Cooper-Williams, E., Herrmann, C., Mata, G., Toovey, A., 2021. Detect, consolidate, delineate: Scalable mapping of field boundaries using satellite images. *Remote Sensing* 13. URL: <https://www.mdpi.com/2072-4292/13/11/2197>, doi:10.3390/rs13112197.
- Wang, S., Waldner, F., Lobell, D.B., 2022. Unlocking large-scale crop field delineation in smallholder farming systems with transfer learning and weak supervision. *Remote Sensing* 14. URL: <https://www.mdpi.com/2072-4292/14/22/5738>, doi:10.3390/rs14225738.
- de Wit, A., Clevers, J., 2004. Efficiency and accuracy of per-field classification for operational crop mapping. *International Journal of Remote Sensing* 25,

4091–4112. doi:[10.1080/01431160310001619580](https://doi.org/10.1080/01431160310001619580).

Yan, L., Roy, D., 2014. Automated crop field extraction from multi-temporal web enabled landsat data. *Remote Sensing of Environment* 144, 42–64. URL: <https://www.sciencedirect.com/science/article/pii/S0034425714000194>, doi:[10.1016/j.rse.2014.01.006](https://doi.org/10.1016/j.rse.2014.01.006).

Zhou, Z.S., Caccetta, P., Devereux, D., Caccetta, M., Woodcock, R., Paget, M., Held, A., 2017. Preparation of analysis ready polsar data for the australian geoscience data cube, in: 2017 IEEE International Geoscience and Remote Sensing Symposium (IGARSS), p. 5229–5232. doi:[10.1109/IGARSS.2017.8128180](https://doi.org/10.1109/IGARSS.2017.8128180).

Zhou, Z.S., Caccetta, P., Furby, S., Mata, G., Lawes, R., 2023. Polarimetric processing and analysis of sentinel-1 time series for state-wide crop mapping in victoria, in: Proc. POLInSAR & BIOMASS 2023, Toulouse.

Appendix A. Sentinel 1 processing

The Entropy/alpha decomposition algorithm was originally developed to simplify the multi-parameter depolarisation issues using statistical method for quad-pol radar backscatter. It can also be applied to the simpler case of dual polarisation. In this latter scenario the radar transmits only a single polarisation and receives, either coherently or incoherently, two orthogonal components of the scattered signal. This corresponds (in the coherent case) to a measurement of the full state of polarisation of the scattered signal for fixed illumination. The current space-borne SAR sensors including Sentinel-1 provide at least a “partial polarimetric mode”, acquiring only 2 of the 4 elements of the Sinclair matrix, for example, HH and HV or VV and VH:

$$\mathbf{S} = \begin{bmatrix} S_{HH} & S_{HV} \\ S_{VH} & S_{VV} \end{bmatrix}. \quad (\text{A.1})$$

The coherent dual-pol Sentinel-1 provides the potential to investigate the development and application of a dual polarised entropy/alpha technique that can be used to take advantage of such coherent dual polarised systems. These radars can be used to estimate the 2x2 wave coherency matrix (Cloude, 2007):

$$\mathbf{J}_H = \begin{bmatrix} \langle S_{HH} S_{HH}^* \rangle & \langle S_{HH} S_{HT}^* \rangle \\ \langle S_{HT} S_{HH}^* \rangle & \langle S_{HT} S_{HT}^* \rangle \end{bmatrix} \quad (\text{A.2})$$

or

$$\mathbf{J}_V = \begin{bmatrix} \langle S_{VV} S_{VV}^* \rangle & \langle S_{VV} S_{VH}^* \rangle \\ \langle S_{VH} S_{VV}^* \rangle & \langle S_{VH} S_{VH}^* \rangle \end{bmatrix}. \quad (\text{A.3})$$

Using the standard interpretation of normalised eigenvalues, λ_i , of \mathbf{J} as probabilities, together with the fact that in 2x2 problems the second eigenvector can be derived from the principal eigenvector using orthogonality, we obtain an Entropy/alpha parameterisation of the wave coherency matrix, \mathbf{J} , as shown in Equations A.4 and A.5:

$$\begin{aligned} \mathbf{J} &= \begin{bmatrix} J_{xx} & J_{xy} \\ J_{xy}^* & J_{yy} \end{bmatrix} \Rightarrow \\ \mathbf{U}_2 &= \begin{bmatrix} \cos \alpha & -\sin \alpha e^{-i\delta} \\ \sin \alpha e^{i\delta} & \cos \alpha \end{bmatrix} \\ \mathbf{D} &= (\lambda_1 + \lambda_2) \begin{bmatrix} P_1 & 0 \\ 0 & P_2 \end{bmatrix} \end{aligned}$$

Expanding the last two equations further yields:

$$\bar{a}_2 = \alpha(P_1 - P_2) + P_2 \frac{\pi}{2} \quad (\text{A.4})$$

$$H_2 = \sum_{i=1}^2 P_i \log P_i \quad (\text{A.5})$$

where \bar{a}_2 and H_2 are defined as the scattering angle and Entropy for the dual-polarised case.

ESA’s SNAP software was used to pre-process all Sentinel-1 products. IW dual-pol images, in both SLC and GRD formats, were processed into analysis-ready data, including normalized radar backscatter coefficients (Γ_0) and polarimetric decomposition parameters, on CSIRO’s HPC systems (Ticehurst et al., 2019; Zhou et al., 2023). The following steps were applied to each dual-pol VV+VH GRD data to generate normalized radar backscatter products: applying the orbit file, removing thermal noise, removing GRD border noise, radiometric calibration, terrain flattening, speckle filtering, multi-looking, and terrain geometric correction. Concurrently, the following steps were implemented for each dual-pol VV+VH SLC data to generate polarimetric decomposition products: applying the orbit file, removing thermal noise, performing radiometric calibration, executing S1 TOPS deburst and merge, calculating polarimetric metrics, applying polarimetric speckle filtering, multi-looking, performing polarimetric decomposition, and terrain geometric correction. The complete workflows for both backscatter and decomposition processing using SNAP on a high-performance computing platform are described in (Zhou et al., 2023). In particular, the implementation of thermal noise removal (Mascolo et al., 2022) and the use of the Copernicus DEM within the data processing have significantly improved the quality of the data for analysis purposes.

Appendix B. Algorithms

Here we present with PYTORCH style pseudocode the implementation of some critical components of the modules we developed.

Appendix B.1. S1 PreProcessing Transformation

Listing 1: Transformation of Sentinel-1 image tiles for deep learning consumption.

```
def transform_s1(s1_tile):
    # Scale angle from degrees to radians
    s1_tile[0] = s1_tile[0] * np.pi / 180.

    # Define symmetric logarithm
    def symlog(x, epsilon=1.e-5):
        return np.sign(x) * np.log(np.abs(x) + epsilon)

    # Apply symlog to VH and VV bands
    for c in [-2, -1]:
        s1_tile[c] = symlog(s1_tile[c])
    return s1_tile
```

Appendix B.2. Raster2Polygons

Listing 2: Conversion of Raster Predictions to Shapefiles.

```
import pandas as pd
import geopandas as gpd
from rasterio import features
from shapely.geometry import shape
import numpy as np
import cv2

def refined_threshold(extent, bounds, t_b, t_e):

    # Threshold and thin the boundary
    tbound = (bound > t_b).astype(np.uint8)
    tbound = cv2.ximgproc.thinning(tbound*255,
                                   cv2.ximgproc.THINNING_GUOHALL)
    tbound = cv2.dilate(tbound, (1,1), iterations=1)

    # Apply refined extent threshold
    thresh = extent * (255 - tbound)
    _, thresh = cv2.threshold(thresh, int(255*thres_ext),
                              255, 0)

    return thresh.astype(np.int16)

def preds2shapes(extent, bounds, t_b, t_e, meta):
    # Obtain refined threshold mask
    thresh = refined_threshold(extent, bounds, t_b, t_e)
    mask = thresh == 255

    # Generate shapes using rasterio
    shapes_rasterio = features.shapes(thresh,
                                       mask=mask, transform=meta['transform'])

    # Convert to DataFrame
    df = pd.DataFrame(shapes_rasterio,
                      columns=['geometry', 'value'])
    df['geometry'] = df['geometry'].apply(shape)

    # Convert to GeoDataFrame
    gdf = gpd.GeoDataFrame(df, geometry='geometry')
    gdf.crs = meta['crs']

    return gdf
```

Appendix C. Modelling Characteristics

We use a Linear warm up scheduler for the first epoch, followed by an annealing cosine strategy with warm restarts (Loshchilov and Hutter, 2017). The initial learning rate was set to $1 \cdot e^{-3}$, the half-life was set to 25 epochs and the period to 50 epochs. For training we used the RAdam optimizer (Liu et al., 2020).

Appendix D. Computational Considerations

For the creation of the ePaddocks product, the PTAViT3D model was trained on 8×V100 (32GB) GPUs with a training chip size of 128×128 pixels. The model consumed 4 time instances of S2 imagery with a batch size of 3 and it was trained for 3 days. Inference was also performed on the same GPUs with up to 16 time instances of S2 observations and batch size of 52 per GPU.